Improving Annual Fine Mineral Dust Representation from the Surface to the Column in GEOS-Chem 14.4.1

Dandan Zhang[1*], Randall V. Martin[1], Xuan Liu[1,2], Aaron van Donkelaar[1], Christopher R. Oxford[1], Yanshun Li[1], Jun Meng[3], Danny M. Leung[4], Jasper F. Kok[5], Longlei Li[6], Haihui Zhu[1], Jay R. Turner[1], Yu Yan[1], Michael Brauer[7], Yinon Rudich[8], and Eli Windwer[8]

[1]Department of Energy, Environmental and Chemical Engineering, Washington University in St. Louis, St. Louis, Missouri 63130, United States

[2]Scripps Institution of Oceanography, University of California San Diego, San Diego, California 92093, United States

[3]Department of Civil and Environmental Engineering, Washington State University, Pullman, Washington 99163, United States

[4]Atmospheric Chemistry Observations and Modeling Laboratory, National Science Foundation National Center for Atmospheric Research, Boulder, Colorado 80301, United States

[5]Department of Atmospheric and Oceanic Sciences, University of California Los Angeles, Los Angeles, California 90095, United States

[6]Department of Earth and Atmospheric Sciences, Cornell University, Ithaca, New York 14853, United States

[7]School of Population and Public Health, University of British Columbia, Vancouver, British Columbia V6T 1Z3, Canada

[8]Department of Earth and Planetary Sciences, Weizmann Institute of Science, Rehovot 76100, Israel

Correspondence to: Dandan Zhang (dandan.z@wustl.edu)

Abstract

Accurate representation of mineral dust remains a challenge for global air quality or climate models due to inadequate parametrization of the emission scheme, removal mechanisms, and size distribution. While various studies have constrained aspects of dust emission fluxes and/or dust optical depth, annual mean surface dust concentrations still vary by factors of 5-10 among models. In this study, we focus on improving the annual simulation of fine dust in the GEOS-Chem chemical transport model, leveraging recent mechanistic understanding of dust source and removal, and reconciling the size differences between models and ground-based measurements. Specifically, we conduct sensitivity simulations using GEOS-Chem in its high performance configuration (GCHP) version 14.4.1 to investigate the effects of mechanism or parameter updates on annual mean concentrations. The results are evaluated by comparisons versus Deep Blue satellite-based aerosol optical depth (AOD) and AErosol RObotic NETwork (AERONET) ground-based AOD for total column abundance, and versus the Surface Particulate Matter Network (SPARTAN) for novel measurements of surface $PM_{2.5}$ dust concentrations. Reconciling modelled geometric diameter versus measured aerodynamic diameter is important for consistent comparison. The two-fold overestimation of surface fine dust in the standard model is alleviated by 39% without degradation of total column abundance by implementing a new physics-based dust emission scheme with better spatial distribution. Further reduction by 20% of the overestimation of surface $PM_{2.5}$ dust is achieved through reducing the mass fraction of emitted fine dust based on the brittle fragmentation theory, and explicit tracking of three additional fine mineral dust size bins with updated parametrization for below-cloud scavenging. Overall, these developments reduce the normalized mean difference against surface fine dust measurements from SPARTAN from 94% to 35%, while retaining comparable skill of total column abundance against satellite and ground-based AOD.

1 Introduction

Mineral dust exerts significant impacts on air quality as the most abundant aerosol component by mass globally (Kok et al., 2021b), on ecosystem health through nutrient transport and deposition such as phosphorous (Bayon et al., 2024; Swap et al., 1992) and iron (Jickells et al., 2005), and on climate through its direct scattering and absorbing of radiation and indirect modifications of cloud properties (Kok et al., 2017; Liao and Seinfeld, 1998; Mahowald et al., 2014). Despite its

importance, accurate representation of long-term concentrations of mineral dust remains a challenge for global air quality or climate models due to inadequate parametrization of the emission scheme (Darmenova et al., 2009; Kok, 2011; Leung et al., 2023), removal mechanisms (Jones et al., 2022; Petroff and Zhang, 2010; Ryu and Min, 2022; Wang et al., 2014b; Zhang and Shao, 2014; Zhang et al., 2001), and size distribution (Kok et al., 2017; Mahowald et al., 2014). Observational constraints from satellite have been applied to reduce the large uncertainty of simulated mineral dust and its emissions (Mytilinaios et al., 2023; Ridley et al., 2016). However, intercomparison projects with various models still suggest large variability within a factor of 2 for the annual mean total column abundance of mineral dust, with even larger variability in surface concentrations and deposition by factors of 5-10 (Huneeus et al., 2011; Uno et al., 2006; Wu et al., 2020).

In addition to total column observations, ground-level measurements of mineral dust offer another promising opportunity to understand mechanisms affecting the accuracy of the surface concentration simulation and the variable performance from the surface to the total column in intercomparison projects. The Surface PARTiculate mAtter Network (SPARTAN, https://www.spartan-network.org/, last access: 4 February 2025) is a globally distributed monitoring network that measures the chemical components of fine particulate matter ($PM_{2.5}$), including in arid environments (Liu et al., 2024; Snider et al., 2015). These ground-based measurements of mineral dust in $PM_{2.5}$ offer new data to evaluate, understand, and improve fine dust simulation in global models.

Dust emissions play a central role in controlling the surface and total column abundance of mineral dust (Kok et al., 2014; Leung et al., 2023; Tian et al., 2021). The predicted spatial distribution of dust emissions particularly affects the downwind dust concentrations through long-range transport and deposition (Prospero, 1999). A new physics-based dust emission scheme (Leung et al., 2023) includes recent developments in the parametrization of the threshold of friction velocity for dust mobilization (Martin and Kok, 2018), combined drag partitioning effects due to rocks (Marticorena and Bergametti, 1995) and vegetation (Pierre et al., 2014a) for a better representation of exerted surface friction velocity (Leung et al., 2023), and intermittent dust mobilization due to high-frequency turbulence (Comola et al., 2019). This dust emission scheme has achieved better spatial correlations of dust column abundance against ground-based and satellite-derived dust optical depth in the Community Earth System Model version 2 (CESM2)

(Leung et al., 2023, 2024). However, the effects of these new developments of dust emission scheme on the bias against ground-based measurements of surface fine dust concentrations are less well known and require further investigation.

The source and removal of dust in the size bins used in dust parametrizations can vary by orders of magnitude across the broad size range of mineral dust (Kok, 2011; Wang et al., 2014b; Zhang et al., 2001). Accounting for this size heterogeneity among dust bins could enable better representation of the global dust cycle. Prior studies have found an underestimation of coarse dust emissions and an overestimation of fine dust (Cakmur et al., 2006; Kok, 2011; Kok et al., 2017). While various studies have focused on developing the representation of coarse or super coarse dust (Kok et al., 2017; Meng et al., 2022), investigation of the effects of different emission size distributions on ambient fine dust are needed through comparison with in situ fine dust measurements. In addition, the developments and improvements of parallel computing in air quality or climate models (Eastham et al., 2018; Harris et al., 2020; Hu et al., 2018; Martin et al., 2022) offer computational capabilities to extend dust size bins with explicit treatments that could enable better representation of dust, especially with rapid variation in processes across different sizes. While the parametrization of dry deposition has been revisited and evaluated against observations (Emerson et al., 2020), below-cloud or washout scavenging has been generally limited to lumped treatments for fine and coarse aerosols in the bulk models (Jones et al., 2022; Wang et al., 2011, 2014a). Developments of the size-resolved parametrization for below-cloud (washout) scavenging (Wang et al., 2014b) are promising to improve the wet deposition of fine dust, which is especially important in distant downwind regions due to long-range transport.

Many studies have examined daily dust variability for the purpose of short-term prediction (Amato et al., 2013; Tindan et al., 2023; Yu et al., 2021). Our study focuses on a different objective of accuracy of annual mean concentrations.

In this study, we implement recent developments of a new dust emission scheme with further refinements including the clay content and wetness in the topsoil layer; reducing the dust emissions over wet, snow and vegetation covered land surfaces; while constraining the global and regional source with satellite aerosol optical depth (AOD). We revisit the size distribution of emitted dust, explicitly track mineral dust with geometric diameter less than 2 μm in four size bins, and update the parametrization for size-resolved washout scavenging. We conduct sensitivity

simulations using the GEOS-Chem chemical transport model in its high performance configuration (GCHP) to investigate the effects of these developments. We focus on improving the annual fine dust representation in GCHP from the surface to the column, by comparisons against ground-level fine dust measurements, and against the ground-based and satellite-retrieved AOD over dusty regions of the Sahara, the Middle East and Asia.

2 Data sources and model description

2.1 Data sources

Ground-based AOD measurements are obtained from the Aerosol Robotic Network (AERONET) Version 3 Level 2 database with improved cloud screening (Giles et al., 2019). The median number of days with AERONET measurements is 168 days for each site. We average daily AERONET AOD to an annual mean in the year of 2018. We use satellite retrievals of AOD from the Deep Blue algorithm (Hsu et al., 2019) based on Collection 6.1 of the Moderate Resolution Imaging Spectroradiometer (MODIS) instrument aboard the satellite platforms of Terra with local overpass around 10:30 and of Aqua around 13:30, and the Version 2.0 Deep Blue aerosol global product of the Visible Infrared Imaging Radiometer Suite (VIIRS) instruments aboard the joint NASA/NOAA Suomi National Polar-orbiting Partnership (Suomi NPP) and NOAA-20 satellites with local overpass around 13:30 (Cao et al., 2014). We choose the Deep Blue aerosol product due to its optimization for the retrieval of aerosol properties over bright surfaces, which is typical over arid regions. We average daily Deep Blue aerosol data for the year 2018. Simulated AOD is coincidently sampled with available daily Deep Blue AOD. We compare simulated AOD over mainly dusty regions (defined as $\mathrm{AOD}_{\mathrm{Dust}}/\mathrm{AOD} > 0.5$ from simulations) against satellite and AERONET AOD to reduce the effects of errors in other AOD components and focus on the performance of mineral dust.

We use the Version 4.2 Level 3 gridded cloud-free tropospheric aerosol extinction profile product during daytime and nighttime of the last 15 years (2007–2021) retrieved from the Cloud–Aerosol Lidar with Orthogonal Polarization (CALIOP) on board the Cloud–Aerosol Lidar Infrared Pathfinder Satellite Observations (CALIPSO) satellite for climatological aerosol profiles (Young et al., 2018).

We use global ground-based data from the Surface Particulate Matter Network (SPARTAN; https://www.spartan-network.org/, last access: 4 February 2025) with filter-based $PM_{2.5}$ chemical composition data (Liu et al., 2024; Snider et al., 2015). Particles with aerodynamic diameter less

than 2.5 μm are collected on Teflon filters using AirPhoton SS5 sampling stations with a sharp-cut cyclone (SCC) 1.829 that operates at a target flow rate of 5 liter per minute (Lpm). The sampling station follows either a standard sampling protocol or the National Aeronautics and Space Administration (NASA) – Italian Space Agency (ASI) Multi-Angle Imager for Aerosols (MAIA) sampling protocol. Under the standard sampling protocol, $PM_{2.5}$ is collected at staggered 3-hour intervals over a 9-day period, generating a 24-hour $PM_{2.5}$ sample covering a full diel cycle. Under the MAIA sampling protocol, $PM_{2.5}$ is collected continuously for 24 hours from 9 am to 9 am at a mission-defined frequency, which has been typically every 3 days during the sampling periods used here. The starting dates for MAIA sites are listed in Table A1. SPARTAN samples are analyzed for fine mineral dust concentrations using X-ray Fluorescence (XRF) and a global mineral dust equation (Equation (A1); Liu et al., 2022) including correction of attenuation effects due to mass loading. The 5-year averaged surface fine dust concentrations from SPARTAN sites are listed in Table A1. We use data from sites with at least 10 samples for the 5-year (2019–2023) period after the network began using XRF with samples. A sensitivity analysis requiring at least 50 samples per site is also conducted. This study used 2,296 filters from 25 SPARTAN sites for a total of 10,072 observational days.

Ground-based observations of $PM_{2.5}$ dust over North America are constructed with a global dust equation (Equation (A1); Liu et al., 2022) and the elemental measurements from the Air Quality System (AQS) database for speciated $PM_{2.5}$ observations in the United States (https://aqs.epa.gov/aqsweb/airdata/download_files.html#Daily, last access: 8 April 2025) and from the National Air Pollution Surveillance Program in Canada (https://data-donnees.az.ec.gc.ca/data/air/monitor/national-air-pollution-surveillance-naps-program/Data-Donnees/2018/?lang=en, last access: 8 April 2025). The AQS database includes measurements from both the Interagency Monitoring of Protected Visual Environments (IMPROVE) and Chemical Speciation Network (CSN) networks.

2.2 GEOS-Chem chemical transport model

We use the GEOS-Chem chemical transport model (http://www.geos-chem.org, last access: 4 February 2025) in its high-performance configuration (Eastham et al., 2018) version 14.4.1 (The International GEOS-Chem User Community, 2024) with improved performance and usability (Martin et al., 2022). The model is driven by meteorological inputs from GEOS Forward Processing (GEOS-FP; https://gmao.gsfc.nasa.gov/, last access: 4 February 2025) with a fine resolution

$0.25^{\circ} \times 0.3125^{\circ}$ (~25 km) and 72 hybrid sigma-pressure vertical levels up to 0.01 hPa. GEOS-FP uses dynamic near-real-time assimilation algorithms compared to consistent static assimilation algorithms used in Modern-Era Retrospective analysis for Research and Applications Version 2 (MERRA-2; https://gmao.gsfc.nasa.gov/GMAO_products/, last access: 19 April 2025). We choose GEOS-FP over MERRA-2 for this study since GEOS-FP offers finer resolution for dust emission calculations.

GEOS-Chem simulates detailed oxidant-aerosol chemistry in the troposphere and stratosphere, with gas-phase mechanism of HO_x-NO_x-BrO_x-VOC-O_3 chemistry (Bey et al., 2001; Wang et al., 2021), coupled to aerosol chemistry for sulfate-nitrate-ammonium (SNA) aerosol (Park et al., 2004), black carbon (BC) (Wang et al., 2014a), and primary and secondary organic aerosol (Pai et al., 2020), sea salt (Jaeglé et al., 2011), and natural and anthropogenic dust (Fairlie et al., 2007; Meng et al., 2021; Philip et al., 2017; Zhang et al., 2013). The gas-aerosol partitioning for SNA is computed by the HETP v1.0 thermodynamic module (Miller et al., 2024). We use the simple, irreversible, direct yield scheme for secondary organic aerosol production (Pai et al., 2020). The effects of aerosol on photolysis rates are computed with relative humidity dependent aerosol size distributions and optical properties for hydrophilic aerosols with improved parametrization for the effective radii of inorganic and organic aerosols (Latimer and Martin, 2019; Ridley et al., 2012; Zhu et al., 2023) and updated optical properties for aspherical hydrophobic mineral dust (http://geoschemdata.wustl.edu/ExtData/CHEM_INPUTS/CLOUD_J/v2025-01/FJX_scat-aer.dat, last access: 7 April 2025) for different dust size bins as calculated by Singh et al. (2024) using the *T*-matrix method for an equiprobable mixture of prolate and oblate spheroids with varying aspect ratios using complex refractive indices from Sinyuk et al. (2003).

The standard dry deposition scheme in GEOS-Chem accounts for gravitational settling, aerodynamic resistance with respect to turbulent transport within the surface layer, and surface resistance to particle-surface contact due to Brownian diffusion, impaction, and interception with an observation constrained parametrization (Emerson et al., 2020; Zhang et al., 2001). Wet deposition includes separate algorithms for scavenging in convective updrafts, and in-cloud and below-cloud scavenging from precipitation (Liu et al., 2001; Wang et al., 2011, 2014a).

Emissions for GEOS-Chem are configured using the Harmonized Emissions Component (HEMCO) module v3.9.1 (Lin et al., 2021). Global anthropogenic emissions are from the Community

Emissions Data System (CEDS) v2 at $0.5^\circ \times 0.5^\circ$ resolution (Feng et al., 2020). Offline emissions of lightning NO_x (Murray et al., 2012), biogenic VOCs, soil NO_x, sea salt (Weng et al., 2020) and mineral dust (Sections 2.3 and 4.2) at $0.25^\circ \times 0.3125^\circ$ resolution are included to represent emission processes at the finest available resolution and to enable consistent emission fluxes across model resolutions. Open fire emissions are from the daily Global Fire Emissions Database (GFED) v4.1s (Giglio et al., 2013) at $0.25^\circ \times 0.25^\circ$ resolution. Other default emission inventories in GCHP v14.4.1 include volcanic SO_2 emissions (Fisher et al., 2011), marine emissions of dimethylsulfide (DMS) (Breider et al., 2017) at $1^\circ \times 1^\circ$ resolution, and ammonia at $0.25^\circ \times 0.25^\circ$ resolution (Bouwman et al., 1997; Croft et al., 2016). We conduct GCHP simulations at C48 (~200 km) resolution for the full year of 2018 following a one-month spin-up.

2.3 Default dust emission scheme

The default dust emission scheme in GEOS-Chem (hereafter GC Dust) originally implemented by Fairlie et al. (2007) is based on the semi-empirical Mineral Dust Entrainment and Deposition (DEAD) emission scheme (Zender et al., 2003) and the GOCART topographical source function (Ginoux et al., 2001) updated to a fine resolution of $0.25^\circ \times 0.25^\circ$ (Meng et al., 2021). The total dust emission flux in kg m^{-2} s^{-1} is calculated based on Zender et al. (2003) and Fairlie et al. (2007):

$$F_d = C_g C_{NA} f_{bare} S \varphi Q_s \quad (1)$$

where C_g is a global scaling factor and C_{NA} is a regional scaling factor in North America for total annual emissions of ~2000 Tg yr^{-1} as optimized by Meng et al. (2021); f_{bare} is the bare ground fraction as specified in Zender et al. (2003) to reduce dust emissions over wet, snow and vegetation covered surfaces:

$$f_{bare} = (1 - A_l - A_{wl})(1 - A_{snow})\left(1 - \frac{\mathrm{LAI}}{\mathrm{LAI}_{\mathrm{thr}}}\right) \quad (2)$$

where A_l, A_{wl}, and A_{snow} is the fraction of land covered by lakes, wetlands, and snow, respectively. LAI is the leaf area index, and $\mathrm{LAI}_{\mathrm{thr}}$ is the threshold LAI to reduce the bare soil fraction due to vegetation cover, which is set to 0.3 m^2 m^{-2} by default.

S is a topographical source function (Ginoux et al., 2001) updated at fine resolution of $0.25^\circ \times 0.25^\circ$ and multiplied by the fraction of bare surface within each grid cell (Meng et al., 2021); φ is the

sandblasting efficiency to convert horizontal saltation flux to vertical dust flux (Marticorena and Bergametti, 1995):

$$\varphi = 10^{13.4 f_{clay} - 4} \quad (3)$$

where f_{clay} is the clay content in the topsoil layer and is set to a global constant value of 0.2 to reduce excessive sensitivity of dust emission fluxes to f_{clay} (Zender et al., 2003). Q_s is the horizontal saltation flux as described in Section A2.

2.4 Size distribution of emitted dust

The default size distribution of emitted dust in GEOS-Chem implemented by Zhang et al. (2013) is based on the Brittle Fragmentation Theory (Kok, 2011) with fitted parameter values for better agreement of dust observations from the Interagency Monitoring of Protected Visual Environments (IMPROVE) ground-based monitoring network in the United States:

$$\frac{dV_d}{d \ln D_d} = \frac{D_d}{c_V}\left[1 + \mathrm{erf}\left(\frac{\ln(D_d/\overline{D_s})}{\sqrt{2}\ln\sigma_s}\right)\right]\exp\left[-\left(\frac{D_d}{\lambda}\right)^3\right] \quad (4)$$

where V_d is the normalized volume for emitted dust aerosols in diameter of D_d in μm; c_V is the normalization constant to make the integration total of V_d of 1; $\overline{D_s} = 3.4$ μm is the median diameter of soil particles; $\sigma_s = 3.0$ is the geometric standard deviation of soil particles; λ is the side crack propagation length, whose value is 8 μm in the default particle size distribution (PSD) used in the GEOS-Chem (GC PSD), and is 12 μm in the Kok PSD (Kok, 2011).

Table 1. The binning of mineral dust in 4-bin and 7-bin simulations using GEOS-Chem. The geometric diameter range is listed in the bracket adjacent to each size bin in unit of μm.

4-bin simulation	7-bin simulation
DST1 (0.2–2.0)	DSTbin1 (0.2–0.36)
	DSTbin2 (0.36–0.6)
	DSTbin3 (0.6–1.2)
	DSTbin4 (1.2–2.0)
DST2 (2.0–3.6)	DSTbin5 (2.0–3.6)
DST3 (3.6–6.0)	DSTbin6 (3.6–6.0)
DST4 (6.0–12.0)	DSTbin7 (6.0–12.0)

Dust aerosols are conventionally separated into several dust bins to compromise between accuracy and computational expense (Ginoux et al., 2001; Zender et al., 2003). Table 1 summarizes the binning of mineral dust in 4-bin and 7-bin simulations. In the GEOS-Chem standard bulk configuration used here, 4 dust size bins are used including DST1 to DST4 covering geometric diameter of 0.2–12.0 μm (Fairlie et al., 2007). For DST1, 4 sub-bins of 0.2–0.36 μm, 0.36–0.6 μm, 0.6–1.2 μm, and 1.2–2.0 μm are further separated for heterogeneous chemistry and AOD calculations, with shared emission, transport and deposition altogether as DST1 (Fairlie et al., 2007). To improve submicron dust representation, we implement full separation of the 7 dust bins for coupled physical and chemical processes in GEOS-Chem, as discussed in Section 4.3.2.

2.5 Reconciling geometric and aerodynamic diameter

A recent study has emphasized the importance of reconciling the geometric diameter used in models and the aerodynamic diameter used in ground-based measurements, especially for mineral dust with higher particle density of ~2500 kg m^{-3} than the standard density of 1000 kg m^{-3} and with aspherical shapes observed in the atmosphere (Huang et al., 2021). We harmonize the differences between geometric diameter and aerodynamic diameter based on Reid et al. (2003):

$$D_{aer} = D_{geo}\sqrt{\frac{\rho_d}{\chi\rho_0}} \quad (5)$$

where D_{aer} is the aerodynamic diameter; D_{geo} is the geometric diameter; $\rho_d = 2500$ kg m^{-3} is the dust density; $\rho_0 = 1000$ kg m^{-3} is the standard spherical particle density; χ is the dynamic shape factor calculated by $\chi = \frac{1}{2}\left(F_s^{1/3} + \frac{1}{F_s^{1/3}}\right)$ and F_s is Stokes form factor (Bagheri and Bonadonna, 2016; Huang et al., 2020) which can be calculated by $\mathrm{HWR}(\frac{1}{\mathrm{AR}})^{1.3}$ where $\mathrm{AR} = 1.70 \pm 0.03$ is the particle length to width ratio, and $\mathrm{HWR} = 0.40 \pm 0.07$ is the particle height to width ratio (Huang et al., 2021). With this conversion, the aerodynamic diameter of 2.5 μm corresponds to the geometric diameter of 1.7 μm. The mass fraction of each simulated dust size bin to the total fine dust mass concentrations can be calculated by the integration of the dust size distribution of Equation (4) with the λ value of 8 μm of the default PSD used in the GEOS-Chem (GC PSD), which is 68% of DST1 with diameter of 0.2–2.0 μm.

In addition to harmonizing different size types used in models and measurements, prior studies also suggested that the sharpness of size cut-off of different inlets used to collect $PM_{2.5}$ samples can affect the measured concentrations (Kenny et al., 2000; Peters et al., 2001). To evaluate the effects, we obtain the dust size distributions of different inlets by multiplying their penetration efficiencies (Peters et al., 2001) and GC PSD (Equation (4)).

Figure 1 shows the effects of the sharpness of size cut on the size distribution of collected dust $PM_{2.5}$ samples. All four inlets have a penetration efficiency of near unity for dust with geometric diameter less than 1.0 μm, which diminishes to 0.5 at a geometric diameter of 1.7 μm and further diminishes with increasing diameter. The Well Impactor Ninety-Six (WINS) referenced by the Federal Reference Method (FRM) exhibits the sharpest size cut. The corresponding dust PSD is sharply attenuated for geometric diameters greater than 1.7 μm. The resultant effects on the mass fractions of the dust size bin to be included in dust $PM_{2.5}$ are small, with the mass fraction of DST1 ranging from 65–70%. The mass fraction based on SCC 1.829 as used by SPARTAN differs by only -0.4% from that based on the original GC PSD without inlet penetration correction. In our Base simulation using the standard version of GEOS-Chem, we calculate surface $PM_{2.5}$ dust as 67.6% of DST1 to account for both aerodynamic diameter and inlet collection efficiency. Neglect of these effects would have increased simulated $PM_{2.5}$ dust concentrations by a factor of 2.

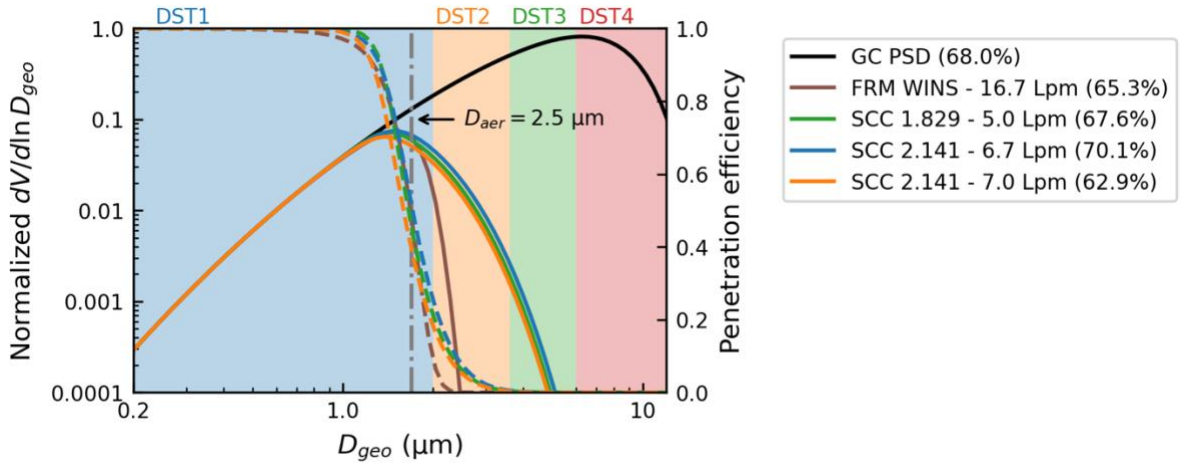

Figure 1. Normalized particle size distribution (PSD) used by default in GEOS-Chem (GC PSD) in solid black with left axis; penetration efficiencies for different types of $PM_{2.5}$ inlets shown in dashed colored lines with right axis, including the Well Impactor Ninety-Six (WINS), and three types of Sharp-Cut Cyclone (SCC) inlets; Solid colored lines show the adjusted GC PSD collected by

different inlets. Grey dash-dotted line indicates the corresponding geometric diameter of 1.7 μm for the aerodynamic diameter of 2.5 μm. Filled rectangles indicate size ranges of 4 dust size bins. Percentages adjacent to GC PSD and different inlets are mass fractions of DST1 for the calculation of $PM_{2.5}$ dust concentrations.

3 Strong overestimation of surface fine dust

Figure 2 shows the spatial distributions of the annual total column AOD and surface $PM_{2.5}$ dust from AERONET, SPARTAN, and the Base simulation using the standard version of GEOS-Chem in the year of 2018. Mineral dust largely determines the AOD in AERONET and GEOS-Chem over and downwind of the main dust source regions including the Sahara, Middle East, and the Taklamakan and Gobi deserts in Asia. The simulated AOD over dusty regions (simulated $\mathrm{AOD_{Dust}}/\mathrm{AOD} > 0.5$) exhibits a high degree of consistency versus the ground-based observations of AERONET AOD with the regression slope near unity and R^2 of 0.7. However, the simulated surface $PM_{2.5}$ dust exhibits a pronounced overestimation by a factor of 2.4 compared to the ground-based measurements of SPARTAN. Simulated $PM_{2.5}$ dust is overestimated at the dusty sites of Abu Dhabi in the United Arab Emirates by 163%, Ilorin in Nigeria by 108%, and Kanpur in India by 96%.

Figure 3 shows the vertical profile of the aerosol extinction normalized by AOD over the main dust source regions and associated downwind regions, to understand the significant performance difference between the surface and the column, with the absolute extinction profile shown in Figure A1. The simulated vertical profile exhibits overall agreement against the 15-year (2007 to 2021) climatological mean extinction vertical profile from the CALIOP, with no evidence of a model overestimate in the lower mixed layer versus aloft, indicating the vertical distribution of mineral dust is not the main driver of the performance discrepancy between the surface and the column. However, further evaluations of the vertical profile near the surface are needed as CALIOP retrievals are challenging at lower altitudes especially below 100 m.

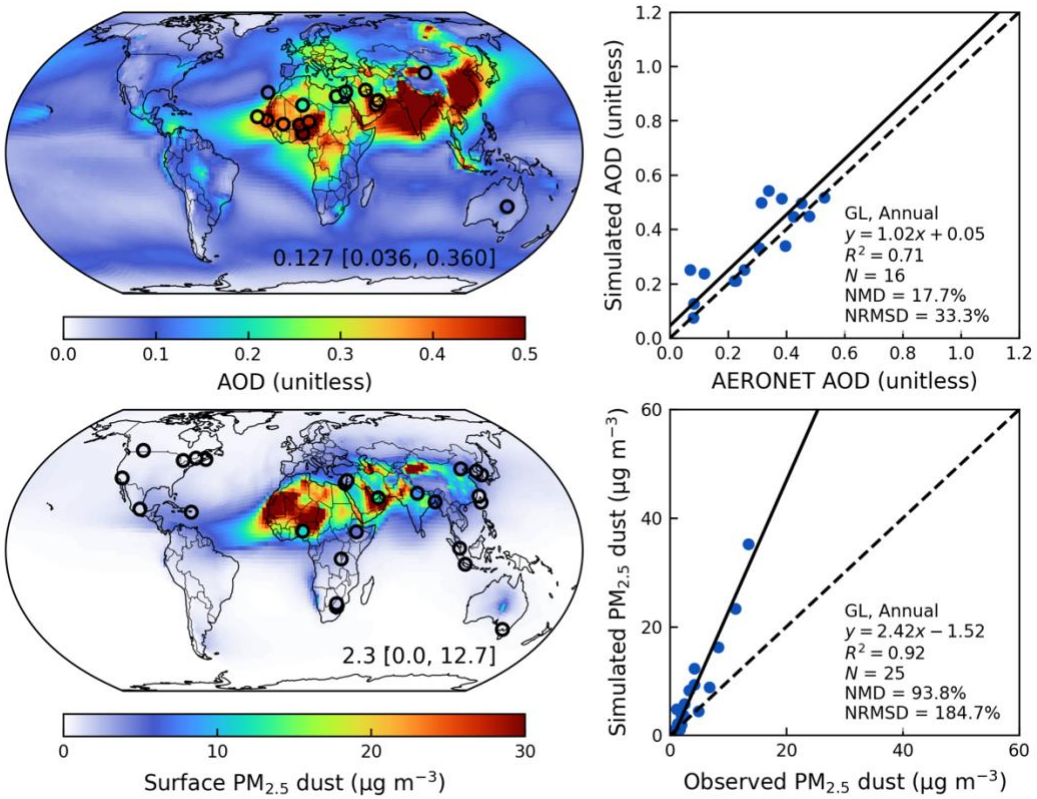

Figure 2. Annual simulated aerosol optical depth (AOD) and comparison against ground-based observations from AERONET over dusty regions (simulated $\mathrm{AOD_{Dust}/AOD} > 0.5$) (top) in the year of 2018; Annual simulated surface $PM_{2.5}$ dust and comparison against ground-based measurements from SPARTAN (bottom) from the Base simulation in the year of 2018. Filled circles on the maps represent ground-based observations from SPARTAN and AERONET. Inset values at the bottom right of the maps are arithmetical mean with 5th and 95th percentiles in the square brackets. Regression statistics including reduced-major-axis linear regression equation, coefficient of variation (R^2), total number of points (N), normalized mean difference (NMD), and normalized root-mean-square difference (NRMSD) are listed at the bottom right of the scatter plots. Major source regions over land are outlined in red including: 1) the Sahara – SA, 2) Middle East – ME, and 3) Asia – AS. Major dust outflow regions over ocean are outlined in green including: 4) the Caribbean Sea – CRB, 5) the tropical Atlantic Ocean – TAT, 6) the Mediterranean Sea – MED, 7) the Arabian Sea – ARB, 8) the tropical Indian Ocean and the Bay of Bengal – IND, and 9) the northwestern Pacific Ocean – NWP.

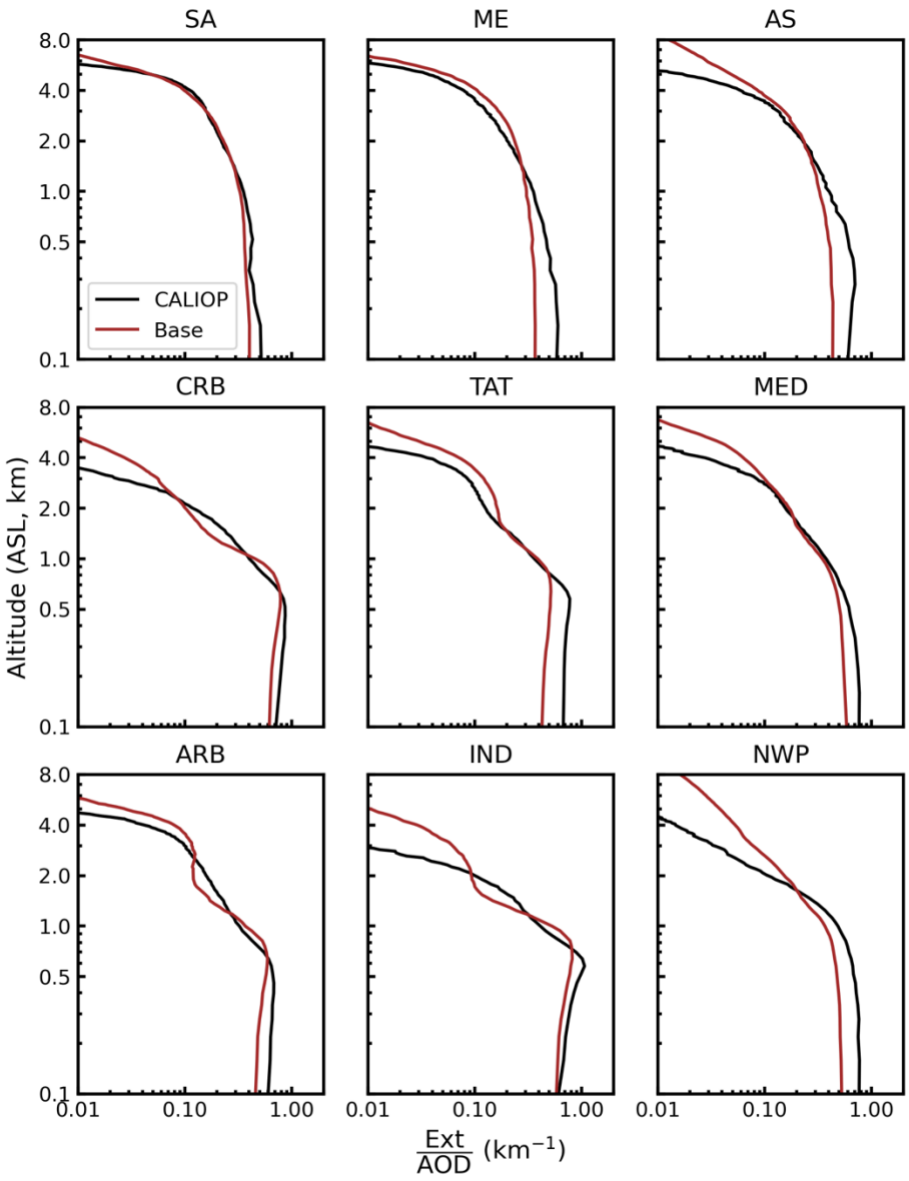

339

340 Figure 3. Comparisons of the annual extinction vertical profile normalized by total column aerosol
341 optical depth from the Base simulation in the year of 2018 against the 15-year (2007 to 2021)
342 climatological mean extinction vertical profile from the CALIOP over different regions including the
343 major dust source regions over land of the Sahara – SA, Middle East – ME, and Asia – AS, and the
344 major dust outflow regions over ocean of the Caribbean Sea – CRB, the tropical Atlantic Ocean –
345 TAT, the Mediterranean Sea – MED, the Arabian Sea – ARB, the tropical Indian Ocean and the Bay of
346 Bengal – IND, and the northwestern Pacific Ocean – NWP.

4 Model revisions to reduce the overestimation of surface fine mineral dust

To reduce the overestimation of surface $PM_{2.5}$ dust, we 1) implement a new dust emission scheme with further refinements for soil properties including the clay content and soil wetness in the top soil layer and the threshold of leaf area index, 2) revisit the size distribution of emitted dust, 3) explicitly track dust with geometric diameter less than 2 μm in four size bins, and 4) update the parametrization for size-resolved below-cloud scavenging.

4.1 Sensitivity simulation setup

Figure 4 summarizes the setup of sensitivity simulations to evaluate the effects of algorithmic modifications and their performance versus satellite-retrieved AOD and surface dust measurements. The default dust simulation (Base) in GEOS-Chem as implemented by Fairlie et al. (2007) uses the DEAD emission scheme (Zender et al., 2003) with a topographical source function (Ginoux et al., 2001; Meng et al., 2021) for natural dust (GC Dust) with 4 dust size bins for emission, transport and removal with 7 dust size bins for dust optical depth calculation and heterogeneous chemistry. To improve the spatial distributions of dust total column abundance, we implement a new dust emission scheme developed by Leung et al. (2023) (DustL23; Emis). Additional modifications on top of the original DustL23 emission scheme include 1) reducing the sensitivity of soil clay content by eliminating the multiplication of the factor of the capped soil clay content f'_{clay} (EmisClay); 2) halving the topmost soil wetness in the layer of 0-5 cm to approximate the soil wetness in the top 1-2 cm layer which is most pertinent to dust emissions (Darmenova et al., 2009; Wu et al., 2022) (EmisClayWet); and 3) reducing the threshold of $\mathrm{LAI}_{\mathrm{thr}}$ from 1.0 m^2 m^{-2} to 0.5 m^2 m^{-2} (EmisClayWetLAI$_{thr}$ or Emis*). To further improve the surface fine dust simulation, we update the GEOS-Chem particle size distribution (PSD) with the PSD developed by Kok et al. (2011) (Emis*PSD) with a larger value for the side crack propagation length of λ (12 μm versus 8 μm) which reduced the mass fraction of emitted fine dust. The Kok PSD was shown to have excellent agreement versus various soil size measurements (Kok, 2011), especially for fine dust distributions (González-Flórez et al., 2023). Lastly, we allow for the four dust bins with geometric diameter less than 2 $\mu\mathrm{m}$ to have separate emission, transport, and dry and wet deposition while halving anthropogenic dust emissions from AFCID (Emis*PSD7Bins0.5AD), and with updated below-cloud or washout scavenging parametrization (Emis*PSD7Bins0.5ADWetDep). Each of these changes is examined below.

The total global annual source strength for each sensitivity simulation is scaled to achieve unity slope versus Deep Blue AOD (Figure A2) over major dust source regions. The surface $PM_{2.5}$ dust concentrations are calculated by accounting for aerodynamic diameter and inlet penetration efficiency (Section 2.5) as 0.676 DST1 for 4-bin simulations, and DSTbin1 + DSTbin2 + DSTbin3 + 0.546 DSTbin4 for 7-bin simulations. We focus our evaluation on the skill in representing in situ $PM_{2.5}$ dust concentrations measured by SPARTAN, and in representing the spatial variation in annual mean AOD. Regression equations are calculated using reduced-major-axis linear regression (Smith, 2009) to account for uncertainties in both simulations and measurements.

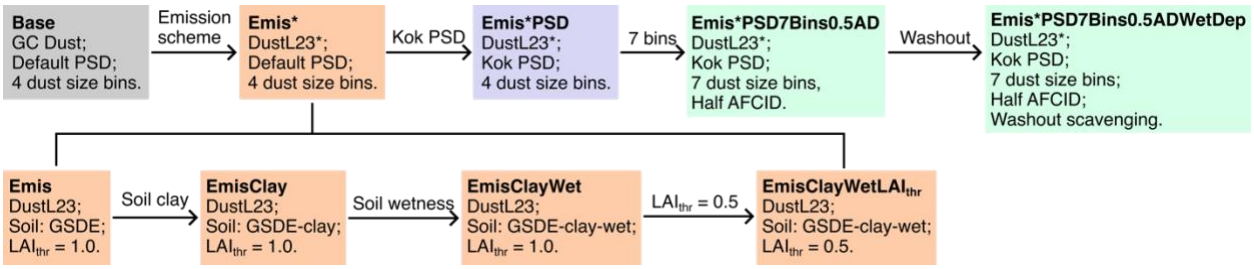

Figure 4. Sensitivity simulation setup. The grey box indicates default settings with the default dust emission scheme used in GEOS-Chem (GC Dust) with 4 dust size bins (Base). The orange box indicates the implementation of a modified dust scheme based on DustL23 (Emis*). Modifications based on the original DustL23 scheme with the soil texture dataset from the Global Soil Dataset for use in Earth System Models (GSDE) (Emis) include the soil clay content (EmisClay), soil wetness (EmisClayWet), and threshold leaf area index ($EmisClayWetLAI_{thr}$). The simulation setup for $EmisClayWetLAI_{thr}$ is the same as that for Emis*. The blue box indicates the modification of size distribution of emitted dust (Emis*PSD). The green boxes indicate the improvements for fine dust including explicit tracking of dust with diameter less than 2 μm with a total of 7 dust size bins with halved anthropogenic fugitive, combustion, and industrial dust (AFCID) emissions (Emis*PSD7Bins0.5AD), and updating below-cloud (washout) scavenging coefficients (Emis*PSD7Bins0.5ADWetDep).

4.2 Improving the spatial distribution of mineral dust with updated emission scheme

We implement into GEOS-Chem a new physics-based dust emission scheme developed by Leung et al. (2023) (DustL23) to replace the default dust emission scheme (Section 2.3) used in GEOS-Chem (GC Dust). The spatial distributions of DustL23 in the Community Earth System Model version 2 (CESM2) exhibited better correlation against dust optical depth datasets and AERONET

AOD than the DEAD scheme (Leung et al., 2024). We modify DustL23 for implementation into GEOS-Chem by 1) reducing dust emissions over wet, snow, and vegetation covered surfaces of semi-arid regions using Equation (7) below, 2) eliminating the multiplication of the capped clay content of the topsoil in Equation (8) below, 3) halving the soil wetness in the layer of 0-5 cm to represent the soil wetness in the top 1-2 cm layer which is most pertinent to dust emissions (Darmenova et al., 2009; Wu et al., 2022), 4) applying a regional scaling factor of 0.6 over the Sahara to reduce its emissions (Equation (8)), and 5) scaling the global total emission flux to achieve unity regression slope of simulated AOD versus Deep Blue AOD over dusty regions.

We begin with the formulation for total dust emission flux F_d in kg m^{-2} s^{-1} following Leung et al. (2024):

$$F_d = \eta C_{tune} C_d f_{bare} f'_{clay} \frac{\rho_a \left(u_{*s}^2 - u_{*it}^2\right)}{u_{*st}} \left(\frac{u_{*s}}{u_{*it}}\right)^{\kappa} \text{ for } u_{*s} > u_{*it} \quad (6)$$

where η is an intermittency factor, C_{tune} is a global tuning factor for the emission strength, C_d is the time-varying soil erodibility coefficient, f_{bare} is the bare ground fraction, f'_{clay} is the clay content in the topmost soil layer of f_{clay} capped at 0.2, ρ_a is the surface air density in kg m^{-3}, u_{*s} is the soil surface friction velocity in m s^{-1} corrected from the surface friction velocity of u_* by the drag partitioning effects of F_{eff}, u_{*it} is the dynamic or impact threshold friction velocity in m s^{-1}, u_{*st} is the standardized wet fluid threshold friction velocity in m s^{-1}, and κ is the fragmentation exponent. We use u_{*st} in the denominator of Equation (6) following Kok et al. (2014) instead of u_{*it} following Leung et al. (2023) for tuning purpose. The parametrization details for these factors following Leung et al. (2023) can be found in Appendix Section A3.

We modify the DustL23 scheme (Leung et al., 2023) by adopting the equation for the bare ground fraction in Zender et al. (2003) to reduce dust emissions over wet, snow and vegetation covered surfaces with the dry erodible land fraction taken from satellite-based land cover:

$$f_{bare} = A_{erod}(1 - A_{snow})\left(1 - \frac{\mathrm{LAI}}{\mathrm{LAI_{thr}}}\right) \quad (7)$$

where A_{erod} is the area fraction of erodible surfaces including barren and sparsely vegetated land cover taken from the MODIS Land Cover Climate Modeling Grid (CMG) (MCD12C1) Version 6.1 data product; A_{snow} is the area fraction of snow cover, LAI is the leaf area index (Yuan et al., 2011), and

$\mathrm{LAI_{thr}}$ is the threshold LAI to reduce the bare soil fraction due to vegetation cover. We set an intermediate value of $\mathrm{LAI_{thr}} = 0.5$ m^2 m^{-2} instead of 1.0 m^2 m^{-2} in Leung et al. (2023) to represent the reduction in dust emissions from sparse vegetation over semi-arid regions, which is more similar to the value of 0.3 used in prior work (Mahowald et al., 1999; Zender et al., 2003).

The enhancement factor $f_m \geq 1$ for the wet fluid threshold friction velocity due to soil wetness is calculated using Equations (A8) and (A9), but with spatially varying clay content f_{clay} in the topsoil layer. The gridded f_{clay} dataset is taken from the Global Soil Dataset for use in Earth System Models (GSDE) with various inputs from global and regional soil database (Shangguan et al., 2014), rather than the machine-learning trained Soil Grids v2.0 dataset with very few observations over arid regions (Poggio et al., 2021) used in Leung et al. (2023). In addition, we reduce the effects of clay content on dust emissions by eliminating the multiplication of the capped clay content f'_{clay}. Soil wetness is taken from the parent meteorological inputs of GEOS-FP (Koster et al., 2020) which targets the top 5 cm layer that desiccates more slowly following precipitation than the soil wetness in the top 1-2 cm layer (Swenson and Lawrence, 2014) that is most pertinent to dust emissions; we halve the soil wetness in an attempt to represent this process (Darmenova et al., 2009; Wu et al., 2022).

The global scaling factor C_{tune} is determined by the reduced-major-axis linear regression slope of simulated AOD versus satellite-retrieved AOD over dusty regions ($\frac{\mathrm{AOD_{Dust}}}{\mathrm{AOD}} > 0.5$) in this study to constrain the intensity of dust emissions, whose values corresponding to different emission schemes are listed in Table A2. Additionally, a regional scaling factor of 0.6 over the Sahara (C_{sah}) and unity elsewhere is applied to reduce regionally excessive dust emissions that may be influenced by the tendency for global models to overrepresent emissions from large source regions compared with smaller sources (Kok et al., 2021a; Zhao et al., 2022).

The final formulation for dust emission flux is:

$$F_d = \eta C_{sah} C_{tune} C_d f_{bare} \frac{\rho_a \left(u_{*s}^2 - u_{*it}^2\right)}{u_{*st}} \left(\frac{u_{*s}}{u_{*it}}\right)^{\kappa} \text{ for } u_{*s} > u_{*it} \quad (8)$$

The calculated offline hourly dust emissions at $0.25^\circ \times 0.3125^\circ$ resolution using Equation (8) are then used to drive GCHP simulations at C48 resolution. The spatial distributions predicted from different emission schemes are evaluated against satellite-based Deep Blue AOD, ground-based

AERONET AOD, and SPARTAN surface $PM_{2.5}$ dust measurements.

Figure 5 shows the spatial distributions of annual dust emission fluxes and dust optical depth predicted from different emission schemes, with Figure 6 showing the comparisons against Deep Blue satellite AOD globally and over major dust source regions. Comparison of the Base and Emis schemes reveals that the latter captures more secondary dust emission spots, especially over the Sahara, and inland dust sources in Saudi Arabia. However, the comparison against Deep Blue AOD over the Sahara is degraded versus the default scheme (Figure 6). As suggested by prior studies, soil clay content is an important factor affecting the threshold friction velocity (Fécan et al., 1999; Tian et al., 2021; Zender et al., 2003) and sandblasting efficiency (Zender et al., 2003), and is often tuned for the optimization of dust emissions (Leung et al., 2024; Tian et al., 2021). Eliminating the multiplication of the capped clay content of f'_{clay} reduces the effects of the clay content, increasing emissions from the Bodélé Depression in Chad and El Djouf across the border of Mauritania and Mali over the Sahara, from the Rub' al Khali desert in the inland Saudi Arabi, and Taklamakan desert in the northwest China (Figure 5, EmisClay). Correspondingly, the R^2 from the linear regression against Deep Blue AOD is improved from 0.60 to 0.70 over the Sahara, from 0.68 to 0.77 over the Middle East, and from 0.35 to 0.56 over Asia (Figure 6). The other two modifications of halving soil wetness (EmisClayWet) and setting LAI_{thr} to 0.5 m^2 m^{-2} ($EmisClayWetLAI_{thr}$) slightly improve the spatial distribution of dust emissions by reducing the underestimation in Asia while retaining the agreements in the Sahara and Middle East (Figure 6). Using the same dusty region of the Base (Figure A3) or $EmisClayWetLAI_{thr}$ (Figure A4) scheme for the comparisons of all dust emission schemes versus Deep Blue AOD confirms similarly slight improvements of regional dust emissions. Together these refinements exhibit comparable global performance as the Base simulation versus Deep Blue AOD with improvements to the relative regional magnitude of dust across the Sahara, Middle East and Asia as indicated by more comparable regression slopes (Figure 6).

Figure 7 shows the evaluation of the Emis* (or $EmisClayWetLAI_{thr}$) simulation with ground-based observations from AERONET and SPARTAN. The overestimation of surface $PM_{2.5}$ dust against the ground-based measurements of SPARTAN is reduced from 94% (Figure 2) to 55% (Figure 7), reflecting regional improvements of the spatial distributions especially over the Middle East (Figure 6). The skill in representing AOD in the Emis* simulation remains comparable to that in the Base simulation shown in Figure 2.

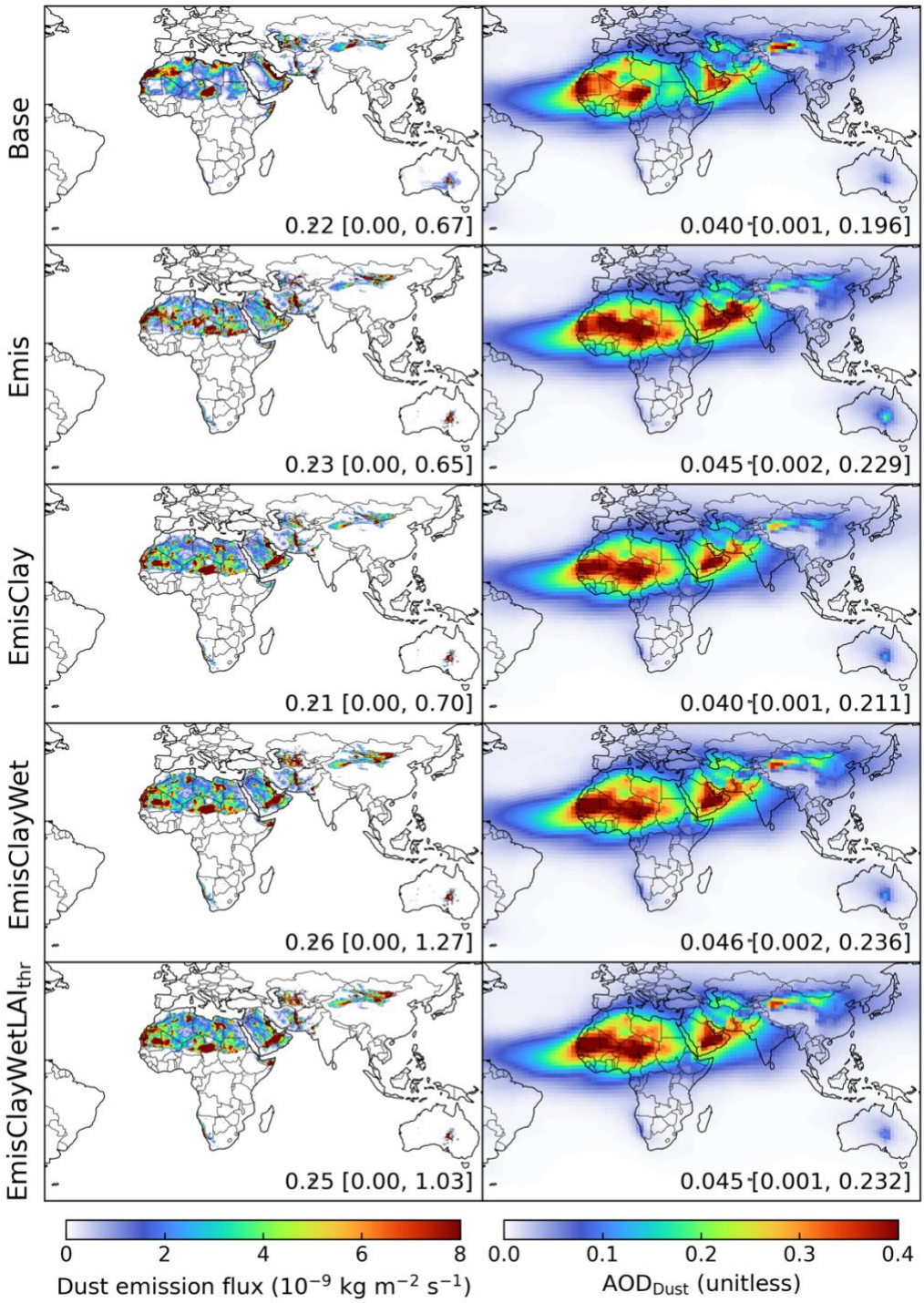

Figure 5. Annual dust emission flux (left) and simulated dust optical depth ($\mathrm{AOD}_{\mathrm{Dust}}$; right) in the year of 2018 zoomed in over dusty regions of the Sahara, Middle East, and Asia from different emission schemes as described in Figure 4. Inset values are the regional arithmetical mean with 5th and 95th percentiles in the square brackets.

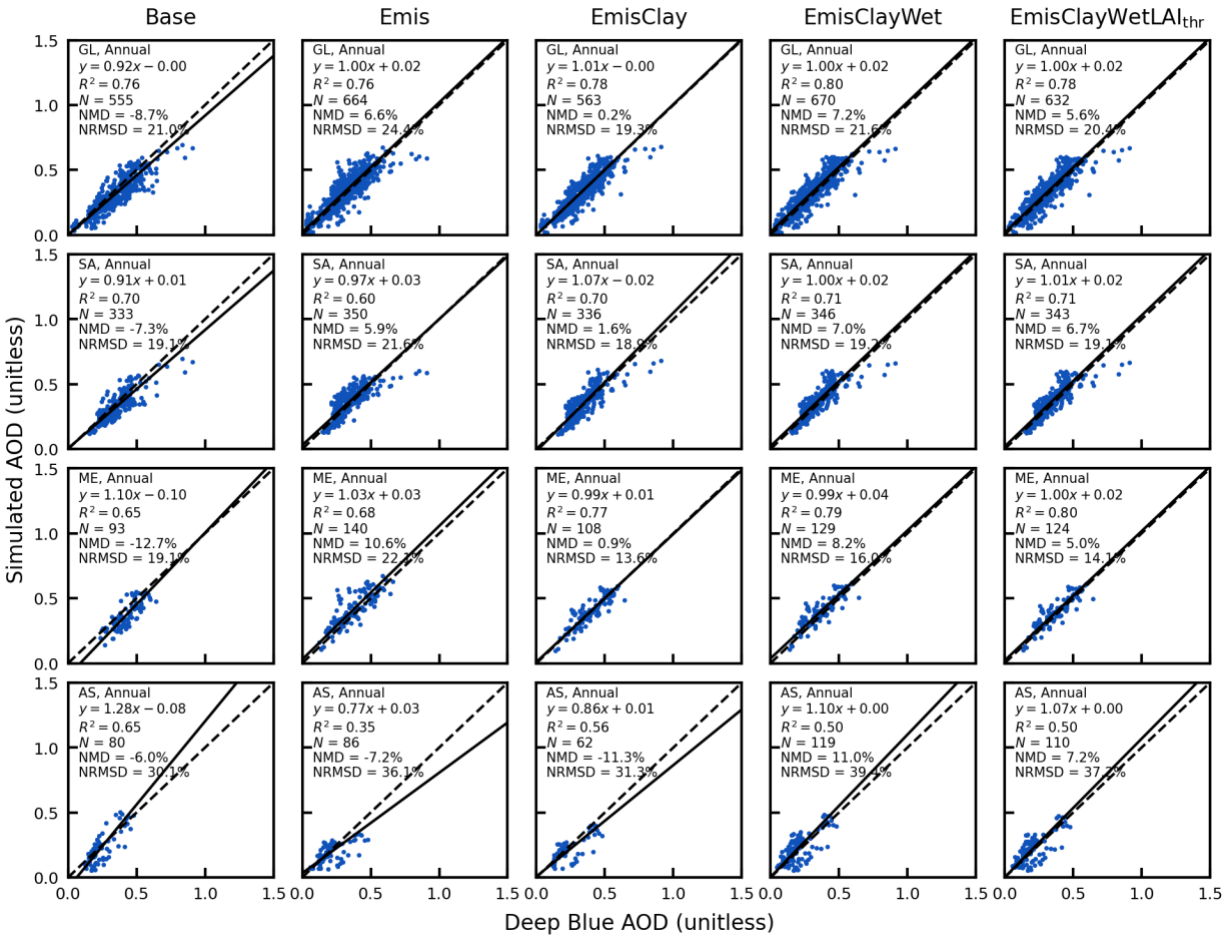

494

495 Figure 6. Comparisons of annual simulated aerosol optical depth (AOD) versus the Deep Blue
496 satellite AOD globally (GL) and over main dust source regions of the Sahara – SA, Middle East – ME,
497 and Asia (AS) with different emission schemes. Regression statistics including reduced-major-axis
498 linear regression equation, coefficient of variation (R^2), total number of points (N), normalized
499 mean difference (NMD), and normalized root-mean-square difference (NRMSD) are in the top left.
500 Note the total number of points varies across different schemes.

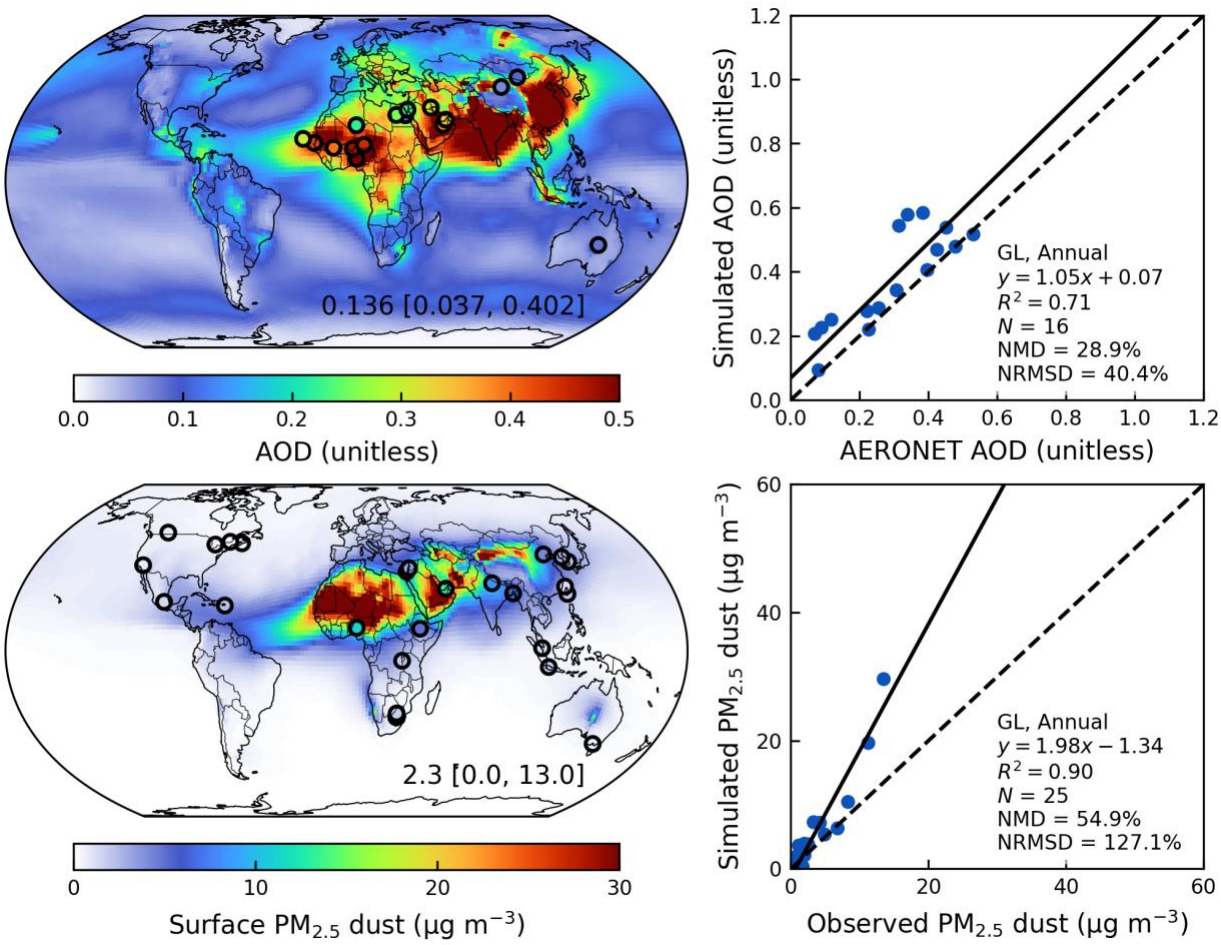

Figure 7. Annual simulated aerosol optical depth (AOD) and comparison against ground-based observations from the AERONET over dusty regions ($\mathrm{AOD_{Dust}/AOD} > 0.5$) (top); Annual simulated surface $PM_{2.5}$ dust and comparison against ground-based measurements from the SPARTAN from the Emis* simulation in the year of 2018 (bottom). Filled circles on the maps represent ground-based observations from SPARTAN and AERONET. Inset values at the bottom right of the maps are arithmetical mean with 5th and 95th percentiles in the square brackets. Regression statistics including the reduced-major-axis linear regression equation, coefficient of variation (R^2), total number of points (N), normalized mean difference (NMD), and normalized root-mean-square difference (NRMSD) are listed at the bottom right of the scatter plots.

4.3 Improving the representation of fine mineral dust

As the size distribution of mineral dust is particularly important for the performance discrepancy between simulated AOD over dusty regions and surface $PM_{2.5}$ dust, we focus on improving its size-

514 resolved source and sink.

515 4.3.1 Revisiting the size distribution of emitted mineral dust

516 Figure 8a shows different PSDs including the default PSD used in the GEOS-Chem (GC PSD) based
517 on the brittle fragmentation theory with the side crack propagation length λ of 8 μm (Zhang et al.,
518 2013), the Kok PSD with λ of 12 μm (Kok, 2011), and the Meng PSD focusing on the optimization for
519 coarse to super coarse dust (Meng et al., 2022), in comparison with the observed PSD from the
520 2011 Fennec campaign (Ryder et al., 2013). While all modelled PSDs are within the wide range of
521 PSD from the Fennec campaign, the fraction of emitted DST1 from the Kok PSD exhibits greater
522 consistency with the Fennec observations than the other two PSDs. The larger discrepancy for the
523 size distribution with diameter less than ~0.4 μm between the observed PSD from Fennec and
524 parametrized PSDs is possibly due to anthropogenic aerosol influence (González-Flórez et al.,
525 2023). In addition, a recent field study in the Moroccan Sahara (González-Flórez et al., 2023)
526 indicated overall agreement of emitted dust size distributions against the Kok PSD especially at the
527 fine diameter range. Therefore, we adopt the Kok PSD with λ of 12 μm for the size distribution of
528 emitted mineral dust in GEOS-Chem. Figure 8b shows the spatial distribution from the Emis*PSD
529 simulation which remains similar to that from the Emis* simulation in Figure 7. Reduced emissions
530 from DST1 by using the Kok PSD reduces the overestimation of surface $PM_{2.5}$ dust from 55% to 33%
531 compared to the ground-based measurements from SPARTAN (Figure 8c).

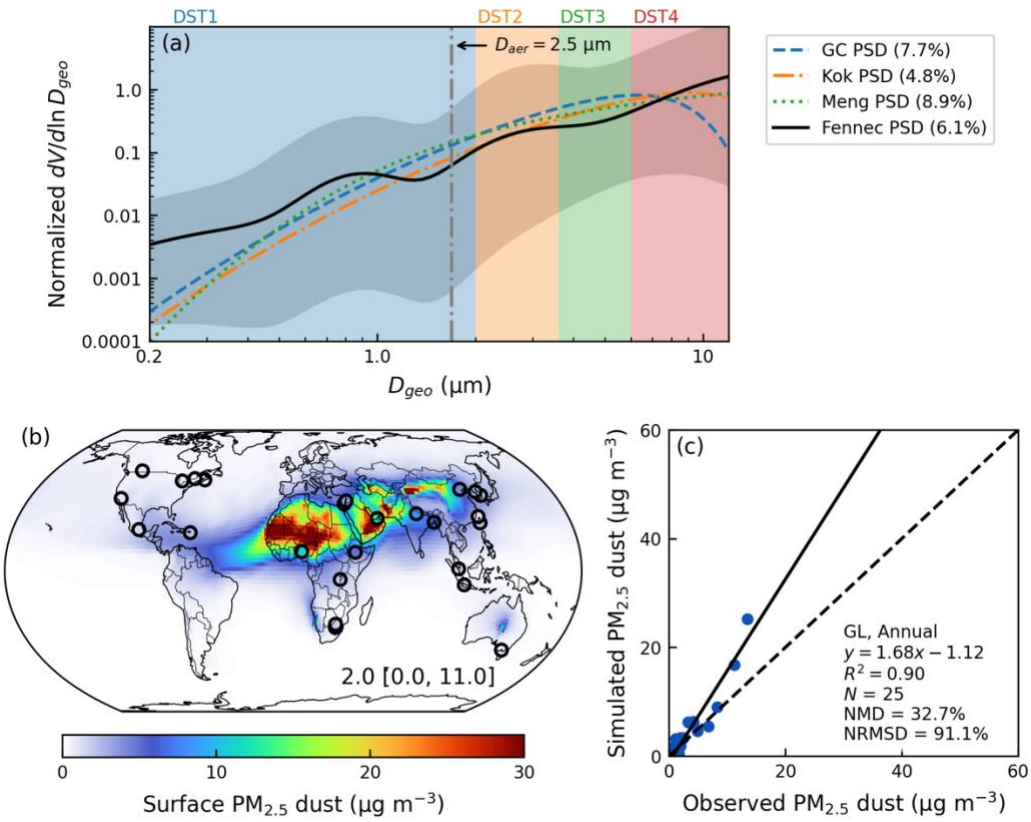

532

533 Figure 8. a) Normalized particle size distribution (PSD) of emitted dust based on default PSD used
534 in GEOS-Chem (GC PSD) (Zhang et al., 2013), the Kok PSD (Kok, 2011), the Meng PSD (Meng et al.,
535 2022), and the Fennec PSD (Ryder et al., 2013). All PSDs are normalized for a total volumetric
536 integration of 1 within the diameter range of 0.2 µm to 12 µm used in GEOS-Chem. The grey shades
537 show the minimum and maximum PSD curves from the Fennec 2011 campaign. The grey dash-
538 dotted line indicates the corresponding geometric diameter of 1.7 µm for the aerodynamic
539 diameter of 2.5 µm. Filled rectangles indicate size ranges of 4 dust size bins. Percentages adjacent
540 to each PSD are mass fractions of emitted DST1 over total dust emission flux within diameter range
541 of 0.2 µm to 12 µm. b) Simulated annual surface $PM_{2.5}$ dust from the Emis*PSD simulation in the
542 year of 2018. Filled circles on the map represent ground-based observations from SPARTAN and
543 AERONET. Inset values at the bottom right of the maps are arithmetical mean with 5th and 95th
544 percentiles in the square brackets. c) Comparison of simulated $PM_{2.5}$ dust versus observed fine
545 dust from SPARTAN. Regression statistics including the reduced-major-axis linear regression
546 equation, coefficient of variation (R^2), total number of points (N), normalized mean difference
547 (NMD), and normalized root-mean-square difference (NRMSD) are listed at the bottom right.

548 4.3.2 Improving the size-resolved dry and wet deposition of mineral dust

549 The default below-cloud (washout) scavenging of dust by rain and snow in GEOS-Chem is
550 separated for fine (DST1) and coarse dust (DST2 to DST4) (Wang et al., 2011). However, washout
551 scavenging coefficients strongly depend on aerosol size (Wang et al., 2014b). To improve the size-
552 dependent washout treatment of dust, we update washout rates by rain and snow for 7 dust size
553 bins by (Wang et al., 2014b):

554 $$\Lambda = A(D_d)(\frac{P_d}{f_r})^{B(D_d)} \quad (9)$$

555 where Λ is the washout scavenging coefficient in s^{-1} by either rain or snow; P_d is the precipitation
556 rate in mm h^{-1} falling form upper layers; f_r is the area fraction of precipitation within each grid box;
557 *A* and *B* are empirical constants dependent on dust size D_d. Using the same semi-empirical
558 equations for *A* and *B* as Wang et al. (2014b), the updated values for different dust size bins with
559 different effective spherical radii are summarized in Table 2.

560 Table 2. Values of *A* and *B* for washout parametrizations by rain and snow for different dust size
561 bins.

Diameter (μm)	Rain ($T \geq 268$ K)		Snow (248 K $\leq T <$ 268 K)	
	A	*B*	*A*	*B*
Bin1 (0.2–0.36)	4.0×10^{-7}	0.71	7.3×10^{-6}	0.57
Bin2 (0.36–0.6)	4.1×10^{-7}	0.71	1.3×10^{-5}	0.56
Bin3 (0.6–1.2)	4.8×10^{-7}	0.72	2.7×10^{-5}	0.56
Bin4 (1.2–2.0)	8.4×10^{-7}	0.73	6.0×10^{-5}	0.55
Bin5 (2.0–3.6)	4.8×10^{-5}	0.88	4.2×10^{-4}	0.61
Bin6 (3.6–6.0)	2.2×10^{-4}	0.87	1.3×10^{-3}	0.67
Bin7 (6.0–12.0)	3.4×10^{-4}	0.84	2.4×10^{-3}	0.73

562

563 Figure 9 shows the size-dependent variations of mineral dust dry and wet deposition. We adopt the
564 effective radii for 7 dust size bins for dry and wet deposition. The dry deposition velocity can vary by
565 a factor of 4.9 among Bin1 to Bin4 with the minimum near the geometric diameter of 0.5 μm. The
566 washout scavenging coefficient can vary by a factor of 2.6 among Bin1 to Bin4 with the minimum

near the geometric diameter of 0.4 μm. Given the steep increasing strength of emitted dust from Bin1 to Bin4 (Figure 8), there is need to explicitly track dust within DST1. We evaluate these developments by examining their effects on the fractional contributions of fine dust to total dust.

Figure 10 shows the fractional contributions of fine dust with geometric diameter less than 2 μm to total dust ($\mathrm{AOD}_{\mathrm{FineDust}}/\mathrm{AOD}_{\mathrm{Dust}}$) from the simulations with a total of 7 dust bins for dry deposition with updated washout scavenging parametrization and their differences. Due to the dominance of dry deposition over arid dusty regions, the explicit tracking of fine dust dry deposition slightly reduces $\mathrm{AOD}_{\mathrm{FineDust}}/\mathrm{AOD}_{\mathrm{Dust}}$ over major dust source regions. However, the anthropogenic contributions to fine dust are correspondingly enhanced over urban and industrial regions, leading to degraded comparison against SPARTAN measurements (Figure A5). We thus halve the AFCID emissions to reduce the excessive contributions from this uncertain source (Emis*PSD7Bins0.5AD). In addition, accounting for the steep washout scavenging efficiency across DSTbin5 to DSTbin7 (Figure 9) with updated washout parametrization would induce enhanced fractional contributions especially for DSTbin5 (Figure A6) and thus relatively reduce fractional contributions from fine dust with geometric diameter less than 2 μm to total dust ($\mathrm{AOD}_{\mathrm{FineDust}}/\mathrm{AOD}_{\mathrm{Dust}}$). Figure 11 shows the overall performance with all revisions from the simulation of Emis*PSD7Bins0.5ADWetDep. The reduced-major-axis linear regression slope is further reduced from 1.68 (Figure 8) to 1.59 with comparable values of NMD against SPARTAN measurements.

Comparisons against other surface dust datasets also show improved or comparable performance compared to the Base simulation. Figure A7 shows the comparison against ground observations over North America. Using the refined new dust emission scheme with the replacement of the size distribution from the Kok PSD, explicitly tracking submicron bins for dry deposition, and updating the washout scavenging parametrization contribute to a comparable extent to reduce the overestimation over North America from 43% of the Base simulation to 15% of the Emis*PSD7Bins0.5ADWetDep simulation. Comparisons against surface concentrations and total deposition of PM_{10} dust (Li et al., 2022b) for the Emis*PSD7Bins0.5ADWetDep simulation are also comparable with the Base simulation (Figures A8 and A9). Consistent with prior studies about the spatial sensitivity of dust emissions (Leung et al., 2023; Meng et al., 2021), fine-resolution meteorological fields are needed to capture dust emission hotspots. If the dust emissions were calculated with C48 meteorological fields, the global dust distribution would become more

concentrated in the major global source regions with the elimination of marginal dust sources, and the R^2 versus SPARTAN surface $PM_{2.5}$ dust would diminish to 0.83 (Figure A10). Overall comparisons for the seasonal mean between the Base and the Emis*PSD7Bins0.5ADWetDep simulations confirm largely reduced overestimation for the surface fine dust against SPARTAN, while retaining comparable skill for the total column AOD against AERONET (Figures A11 to A14). The reduction of surface overestimation is especially prominent over dusty seasons in Spring (from 73% to 48%) and Summer (from 138% to 50%), while further improvements are needed for surface overestimation in Fall (from 140% to 95%).

Table 3 summarizes the effects of different modifications on the model performance of total column AOD and surface fine mineral dust in this study. Strong overestimation of surface $PM_{2.5}$ dust concentrations exist in the Base simulation by a factor of 2.4 versus SPARTAN measured dust. Updating the dust emission scheme with further refinements in the soil properties reduces the overestimation of surface $PM_{2.5}$ dust by 39%. The surface overestimation by 55% is reduced to 35% by updating the size distribution of emitted dust, explicitly tracking dust with diameter less than 2 μm in 4 bins, and updating the parametrization of below-cloud scavenging. The comparisons of simulated AOD versus AERONET and Deep Blue AOD are comparable for all simulations with the correlation coefficient of 0.8-0.9, and NMDs from −9% to 31%. The emissions between the Base and Emis* simulations are comparable with the global annual dust emission of ~2000 Tg yr^{-1}, which is within the range of 1000-5000 Tg yr^{-1} from intercomparison projects (Huneeus et al., 2011; Wu et al., 2020). As the Kok PSD reduces the mass fraction of fine dust, the total emitted mass is enhanced to ~3000 Tg yr^{-1} with larger contributions from coarse dust. The reduction of surface $PM_{2.5}$ dust overestimation with these revisions is confirmed if SPARTAN sites are restricted to those with at least 50 samples as well (Table A3).

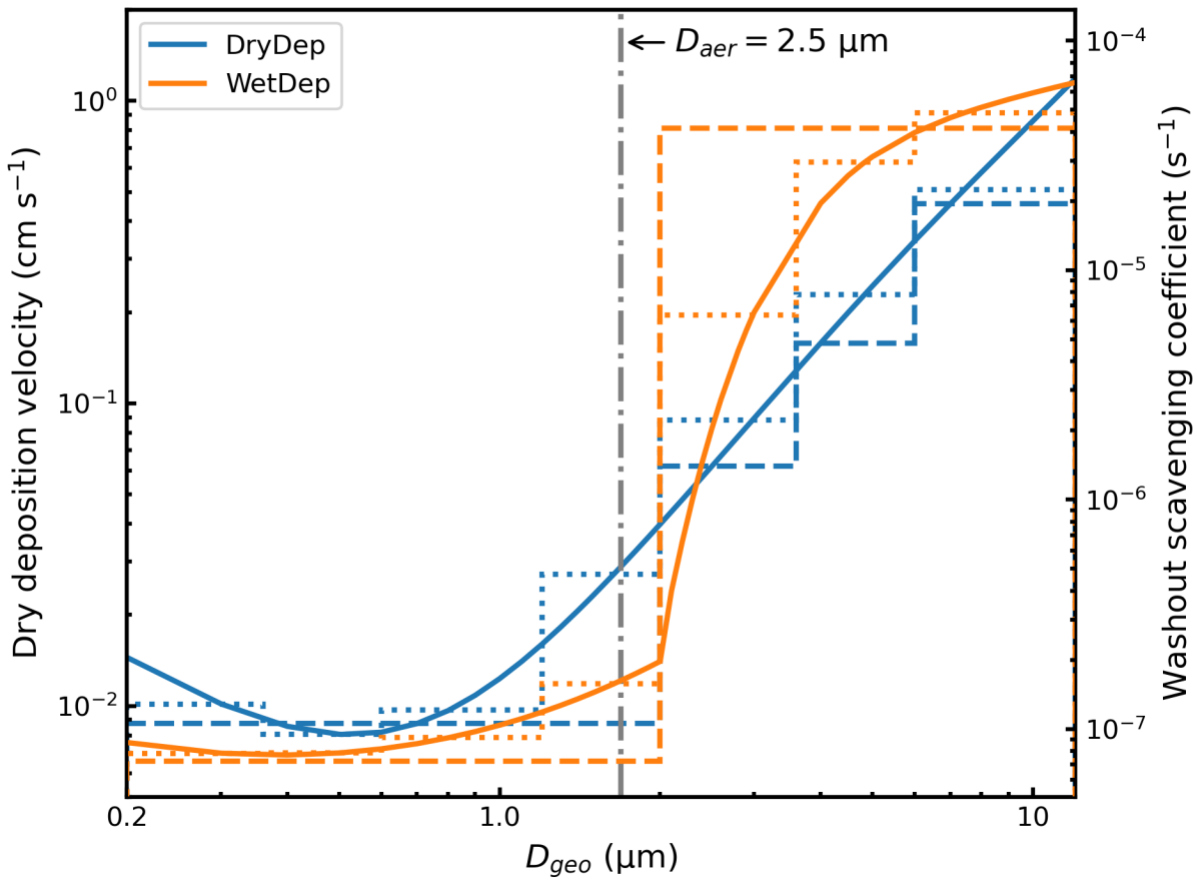

622

623 Figure 9. Size-resolved dry deposition velocity over desert (left y-axis) and washout scavenging
624 coefficient by rain (right y-axis). Dry deposition velocity is calculated with the friction velocity of 0.4
625 $\mathrm{m\ s^{-1}}$ and the particle density of 2500 $\mathrm{kg\ m^{-3}}$ with the default dry deposition scheme used in the
626 GEOS-Chem. Washout scavenging coefficient is calculated with the precipitation rate of 0.1
627 $\mathrm{mm\ h^{-1}}$ with the updated washout parametrization. Solid lines indicate theoretical
628 parametrization. Dashed lines indicate the default discrete treatment. Dotted lines indicate the
629 updated discrete treatment. Grey dash-dotted line indicates the corresponding geometric
630 diameter of 1.7 μm for the aerodynamic diameter of 2.5 μm.

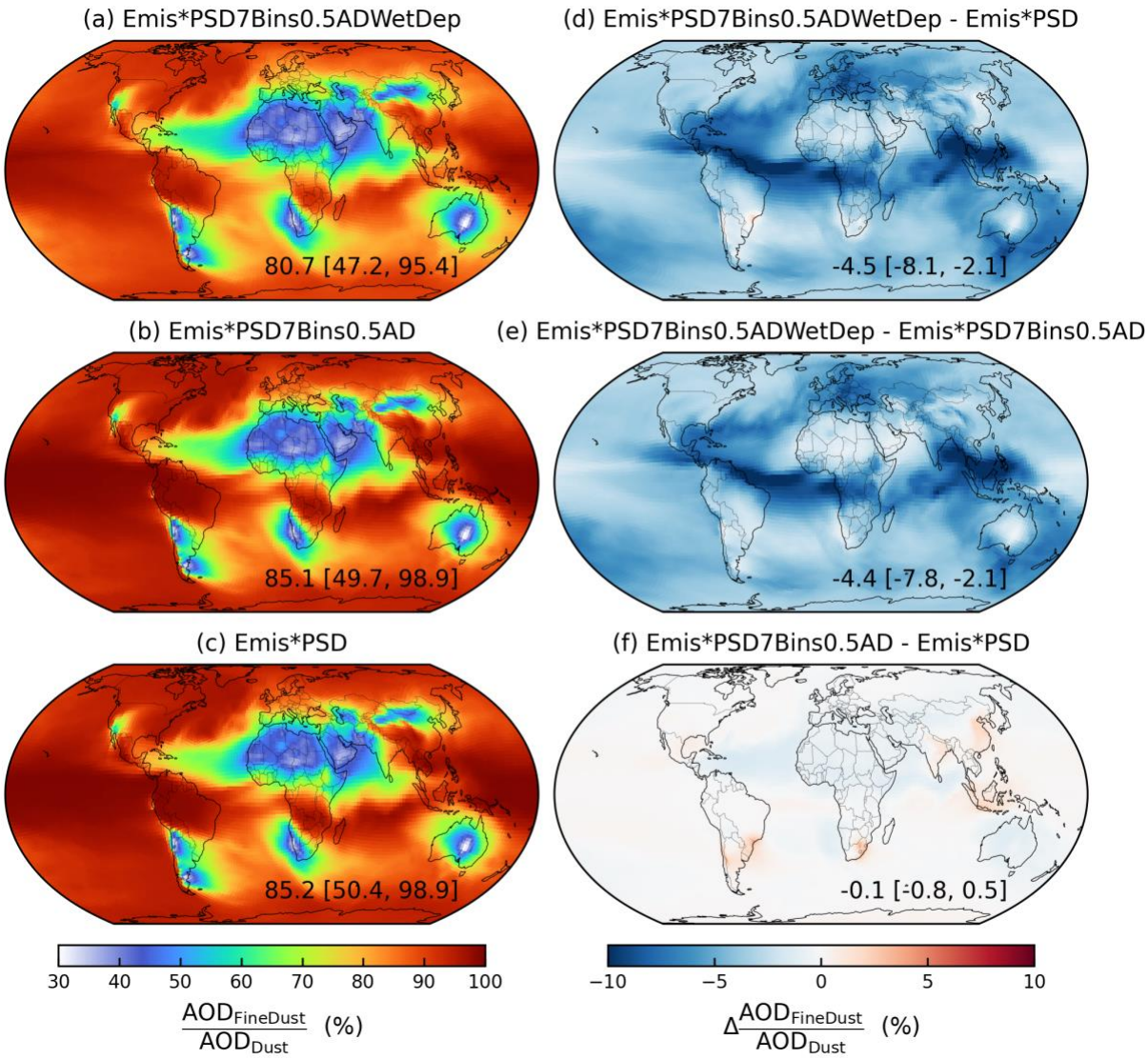

631

632 Figure 10. Fractional contributions of fine dust with geometric diameter less than 2 μm to total dust
633 column abundance ($\mathrm{AOD_{FineDust}}/\mathrm{AOD_{Dust}}$) from the a) Emis*PSD7Bins0.5ADWetDep, b)
634 Emis*PSD7Bins0.5AD, c) Emis*PSD and their absolute differences. Inset values at the bottom right
635 are arithmetical mean with 5th and 95th percentiles in the square brackets.

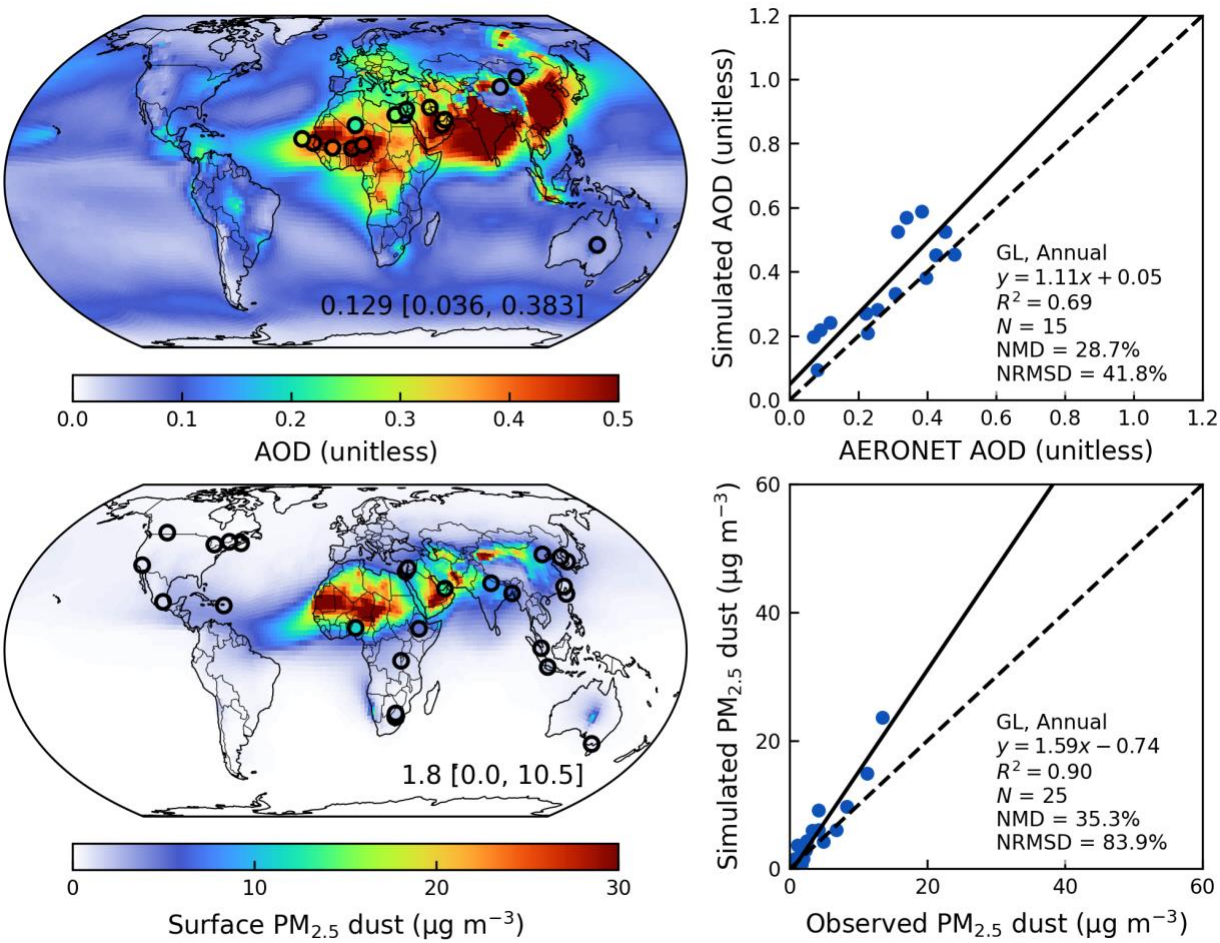

Figure 11. Annual simulated aerosol optical depth (AOD) and comparison against ground-based observations from AERONET over dusty regions ($\mathrm{AOD_{Dust}}/\mathrm{AOD} > 0.5$) (top); Annual simulated surface $PM_{2.5}$ dust and comparison against ground-based measurements from SPARTAN from the Emis*PSD7Bins0.5ADWetDep simulation in the year of 2018 (bottom). Filled circles on the maps represent ground-based observations from SPARTAN and AERONET. Inset values at the bottom right of the maps are arithmetical mean with 5th and 95th percentiles in the square brackets. Regression statistics including the reduced-major-axis linear regression equation, R^2, total number of points (N), normalized mean difference (NMD), and normalized root-mean-square difference (NRMSD) are listed at the bottom right of the scatter plots.

Table 3. Effects of different modifications on the model performance of simulated annual surface $PM_{2.5}$ dust versus SPARTAN, and simulated annual aerosol optical depth (AOD) versus AERONET AOD and Deep Blue satellite AOD in terms of the correlation coefficient (*r*), the reduced-major-axis linear regression slope, and the normalized mean difference (NMD), with associated annual dust optical depth (AOD_{Dust}) and total dust emissions in the year of 2018.

Simulation	Simulated surface $PM_{2.5}$ dust versus SPARTAN			Simulated AOD versus AERONET AOD			Simulated AOD versus Deep Blue AOD			AOD_{Dust} (unitless)	Emissions ($Tg\ yr^{-1}$)
	r	slope	NMD (%)	*r*	slope	NMD (%)	*r*	slope	NMD (%)		
Base	0.96	2.42	93.8	0.84	1.02	17.7	0.87	0.92	-8.7	0.025	2025
Emis*											
Emis	0.96	1.96	65.8	0.85	1.10	26.2	0.87	1.00	6.6	0.028	2128
EmisClay	0.95	1.85	34.3	0.86	1.05	23.7	0.88	1.01	0.2	0.025	1954
EmisClayWet	0.95	2.03	63.3	0.87	1.11	30.7	0.89	1.00	7.2	0.029	2376
EmisClayWetLAI_{thr}	0.95	1.98	54.9	0.85	1.05	28.9	0.88	1.00	5.6	0.028	2262
Emis*PSD	0.95	1.68	32.7	0.83	1.12	29.7	0.89	1.00	4.3	0.026	3069
Emis*PSD7Bins0.5AD	0.95	1.63	40.6	0.85	1.12	28.3	0.89	1.00	3.2	0.026	2952
Emis*PSD7Bins0.5ADWetDep	0.95	1.59	35.3	0.83	1.11	28.7	0.89	1.00	3.6	0.026	2943

5 Conclusions

In summary, we evaluate and improve the annual mineral dust simulation in the GEOS-Chem model by building upon recent ground-based measurements from SPARTAN of mineral dust in $PM_{2.5}$ over land, together with total column AOD from AERONET measurements and from the MODIS and VIIRS Deep Blue satellite products. We devote attention to the representation of aerodynamic diameter when comparing with ground-based $PM_{2.5}$ measurements, since representation as geometric diameter in models would introduce a two-fold bias. We nonetheless find that the standard GEOS-Chem chemical transport model much better represents columnar AOD with a slope near unity than surface $PM_{2.5}$ dust concentrations which are overestimated by a factor of two. Comparison of simulated extinction profiles versus the 15-year climatological CALIOP extinction profiles yields overall consistency in the vertical shape (Figure 3), indicating the importance of other dominant factors.

We develop the mineral dust representation in GEOS-Chem with attention to its sources, size distribution, and sinks. We implement a new dust emission scheme based on Leung et al. (2023) with further refinements to the clay content and wetness in the topsoil layer, threshold leaf area index, and reducing dust emissions over snow and vegetation covered land surfaces. The NMD versus surface measurements is reduced by 39% while the simulated AOD better represents the spatial distribution of Deep Blue AOD over dusty regions. To further improve the fine dust representation in GEOS-Chem, we revisit the size distribution of emitted dust and find that the Kok particle size distribution (PSD; Kok, 2011) better represents the mass fraction of fine dust measured during the Fennec field campaign over Northern Africa than does the default PSD despite the uncertainties from the Fennec observations. The implementation of the Kok PSD into GEOS-Chem reduces the surface overestimation of $PM_{2.5}$ dust by 22%. We also enable explicit tracking of mineral dust with geometric diameter less than 2 μm in 4 size bins for emission, transport, and deposition with updated parametrization for below-cloud scavenging, which further reduces the overestimation of surface $PM_{2.5}$ dust concentrations to within 35%.

Despite these advances, challenges remain in mineral dust development and evaluation. The performance of AOD against satellite and AERONET observations over dusty regions may still be affected by other aerosol components which may benefit from further evaluations and developments. Although the simulations are only for a single year, we average the multi-year

observational data from the CALIOP extinction profile and SPARTAN measured surface dust concentrations for long-term representativeness. This approach benefits from the weak interannual variability of annual mean mineral dust concentrations (Li et al., 2017; Song et al., 2021). Nonetheless, additional observational data will enable further evaluation of the performance of mineral dust simulations. In addition, knowledge gaps remain for mechanistic representation of mineral dust emissions. We call for further developments on the parametrization of dust emissions, particularly for the uncertainties in global and regional dust emission strength and further constraints on the effects of soil wetness on the threshold friction velocity. Future examination of daily variability would also be valuable for short-term predictability.

These investigations indicate the importance of size type reconciliation in models versus measurements, the spatial distribution of dust emissions, the size distribution of emitted dust, and the explicit tracking of fine dust bins for more accurate simulation of fine dust abundance from the surface to the column.

Appendix A: Additional details about dust emission parametrizations, SPARTAN dust, and complementary figures

A1. A global dust equation

We follow a global dust equation for the calculation of surface $PM_{2.5}$ dust concentrations from SPARTAN (Liu et al., 2022):

$$\text{Dust} = [1.89\text{Al} \times (1 + \text{MAL}) + 2.14\text{Si} + 1.40\text{Ca} + 1.36\text{Fe} + 1.67\text{Ti}] \times \text{CF} \quad \text{(A1)}$$

where 1.89, 2.14, 1.40, 1.36, and 1.67 are the mass conversion ratios for corresponding mineral oxides; MAL is the mineral-to-aluminum mass ratio of $(K_2O + MgO + Na_2O)/Al_2O_3$; CF is a correction factor (CF) to account for other missing compounds.

A2. Horizontal saltation flux in standard version of GEOS-Chem

The default horizontal saltation flux Q_s in GEOS-Chem is based on the parametrization of White (1979):

$$Q_s = C_z \frac{\rho_a}{g} u_{*s}^3 \left(1 - \frac{u_{*ft}}{u_{*s}}\right)\left(1 + \frac{u_{*ft}}{u_{*s}}\right)^2 \text{ for } u_{*s} > u_{*ft} \quad \text{(A2)}$$

where $C_z = 2.61$ is the saltation constant; ρ_a is the air density in kg m^{-3}; $g = 9.81$ m s^{-2} is the gravitational acceleration; the drag partitioning effects are ignored by default and thus $u_{*s} = u_*$, where u_* is calculated from the wind speed at 10 m u_{10m} based on the logarithmic wind profile within the boundary layer under adiabatic conditions (Marticorena and Bergametti, 1995):

$$u_* = \frac{k u_{10m}}{\ln(z_0/z_{0a})} \tag{A3}$$

where $k = 0.4$ is the von Kármán constant; u_{10m} is the wind speed at 10 m; $z_0 = 10$ m is the reference height; $z_{0a} = 10^{-4}$ m is the surface roughness height. The wet fluid threshold friction velocity of u_{*ft} is the minimum surface friction velocity required to initiate the saltation from the bare soil (Fécan et al., 1999):

$$u_{*ft} = u_{*ft0} \cdot f_m \tag{A4}$$

where u_{*ft0} is the dry fluid threshold friction velocity following Iversen and White (1982):

$$u_{*ft0} = \begin{cases} \dfrac{0.129K}{\sqrt{1.928Re^{0.092} - 1}}, & 0.03 < Re < 10 \\ 0.12K[1 - 0.0858e^{-0.0617(Re-10)}], & Re \geq 10 \end{cases} \tag{A5}$$

where:

$$K = \sqrt{\frac{\rho_p g D_p}{\rho_a}\left(1 + \frac{0.006}{\rho_p g D_p^{2.5}}\right)} \tag{A6}$$

$$Re = 1331 D_p^{1.56} + 0.38 \tag{A7}$$

Where $D_p = 75$ μm is the diameter of soil particle which corresponds to the minimum dry fluid threshold velocity of u_{*ft0} (Iversen and White, 1982).

The enhancement factor $f_m \geq 1$ is a function of soil wetness (Fécan et al., 1999):

$$f_m = \begin{cases} 1, & w \leq w_t \\ \sqrt{1 + 1.21[100(w - w_t)]^{0.68}}, & w > w_t \end{cases} \tag{A8}$$

where w is the gravimetric soil moisture (kg kg^{-1}) in the shallowest soil layer; w_t is the threshold

gravimetric water content above which u_{*ft} increases with soil wetness (Fécan et al., 1999):

$$w_t = 0.01a\left(17f_{clay} + 14f_{clay}^2\right) \quad \text{(A9)}$$

where a is a tuning factor which is taken as $1/f_{clay} = 5$ by default.

A3. Additional details about the new dust emission scheme

The variables used in the calculation for the total dust emission flux F_d (Equation (6)) can be categorized into meteorological fields including η, ρ_a, and u_*, land surface properties including f_{bare}, f'_{clay}, F_{eff}, and u_{*it}, intrinsic soil erodibility properties including u_{*st}, C_d, and κ, and a global tuning factor of C_{tune}.

Intermittency effects due to the fluctuation of instantaneous soil friction velocity $\tilde{u}_s$ are reflected in the intermittency factor of η, which is denoted by the temporal fraction of active dust emission ranging from 0 to 1 within a transport time step. The parametrization of η is based on Comola et al. (2019):

$$\eta = 1 - P_{ft} + \alpha\left(P_{ft} - P_{it}\right) \quad \text{(A10)}$$

where P_{ft} and P_{it} are the cumulative probability of instantaneous friction velocity larger than a wet fluid threshold, and an impact threshold, respectively; α is the fraction of $\tilde{u}_s$ crossing a wet fluid threshold over the total fraction crossing a wet fluid threshold and an impact threshold.

The calculation of η is based on velocity at the saltation height of $z_{sal} = 0.1$ m. Thus the surface friction velocity of u_{*s}, and threshold velocities of u_{*ft} and u_{*it} are first calculated at the saltation height based on (Marticorena and Bergametti, 1995):

$$u_X(sal) = \frac{u_{*X}}{k}\ln\left(\frac{z_{sal}}{z_{0a}}\right) \quad \text{(A11)}$$

where the subscript *X* can be *ft*, *it* or *s*, $z_{0a} = 10^{-4}$ m, and $k = 0.386$ is the von Kármán constant.

Assuming a normal distribution of instantaneous soil friction velocity $\tilde{u}_s \sim \mathrm{N}(u_s, \sigma^2_{\tilde{u}_s})$, a standard deviation of instantaneous friction velocity $\sigma_{\tilde{u}_s}$ is a central parameter to calculate the fraction of active dust emissions within a time step for transportation. $\sigma_{\tilde{u}_s}$ is calculated based on the similarity

theory (Panofsky et al., 1977):

$$\sigma_{\tilde{u}_s} = u_{*s}\left(12 - 0.5\frac{z_i}{L}\right)^{1/3} \quad \text{(A12)}$$

where z_i is the planetary boundary layer height, and L is the Monin-bukhov length calculated by (Panofsky et al., 1977):

$$L = -\frac{\rho_a c_p T u_*^3}{kgH} \quad \text{(A13)}$$

where $c_p = 1005\ \mathrm{J\ kg^{-1}K^{-1}}$ is the specific hear capacity of air under constant pressure; T is surface air temperature; u_* in m s^{-1} is the original surface friction velocity without the drag partitioning correction; $\mathrm{g} = 9.81\ \mathrm{m\ s^{-2}}$ is the gravitational acceleration; H is the sensible heat flux from turbulence in W m^{-2}.

Given that a normal distribution is assumed, cumulative probabilities of P_{ft} and P_{it} can be calculated by $P_{ft} = 0.5[1 + \mathrm{erf}\,(\frac{u_{ft}-u_s}{\sqrt{2}\sigma_{\tilde{u}_s}})]$, and $P_{it} = 0.5[1 + \mathrm{erf}\,(\frac{u_{it}-u_s}{\sqrt{2}\sigma_{\tilde{u}_s}})]$. α is the number of crossing rate of $\tilde{u}_s$ across the wet fluid threshold C_{ft} over the total number of crossing rate of $\tilde{u}_s$ across the wet fluid threshold C_{ft} and the impact threshold C_{it} (Comola et al., 2019):

$$\alpha = \frac{C_{ft}}{C_{ft} + C_{it}} \quad \text{(A14)}$$

The crossing fraction of α is approximated by $\alpha \approx [\exp\left(\frac{u_{ft}^2 - u_{it}^2 - 2u_s(u_{ft}-u_{it})}{2\sigma_{\tilde{u}_s}^2}\right) + 1]^{-1}$ as suggested by Comola et al. (2019).

The soil surface friction velocity of u_{*s} is calculated by (Leung et al., 2023; Marticorena and Bergametti, 1995; Webb et al., 2020):

$$u_{*s} = u_* F_{eff} \quad \text{(A15)}$$

where u_* is the surface friction velocity taken directly from the parent meteorological fields; F_{eff} is the drag partitioning effects due to the presence of non-erodible elements including rocks and vegetation.

Drag partitioning effects are calculated following Leung et al. (2023):

$$F_{eff} = \left(A_r f_{eff,r}^3 + A_v f_{eff,v}^3\right)^{1/3} \tag{A16}$$

where A_r is the fraction of barren and sparsely vegetated land cover approximated by A_{erod}; A_v is the fraction of short vegetation land cover taken from the MCD12C1 Version 6.1 land cover product; $f_{eff,r}$ is the drag partitioning effects due to rocks (Marticorena and Bergametti, 1995):

$$f_{eff,r} = 1 - \frac{\ln\left(\frac{z_{0a}}{z_{0s}}\right)}{\ln\left[b_1\left(\frac{X}{z_{0s}}\right)^{b_2}\right]} \tag{A17}$$

where z_{0a} is the aeolian roughness length which the surface roughness of overlaying nonerodable elements and was taken as the minimum of monthly mean gridded aeolian roughness length (Prigent et al., 2005); $z_{0s} = \frac{D_p}{15}$ is the smooth roughness length which quantifies the roughness of a bed of fine soil particles in the absence of roughness elements (Pierre et al., 2014b); $b_1 = 0.7$, $b_2 = 0.8$, and $X = 10$ m are empirical constants (Leung et al., 2023). $f_{eff,v}$ is the drag partitioning effects due to vegetation (Pierre et al., 2014a):

$$f_{eff,v} = \frac{K + f_0 c}{K + c} \tag{A18}$$

where $f_0 = 0.32$ and $c = 4.8$ are empirical constants (Okin, 2008); K is calculated by $\frac{\pi}{2}\left(\frac{1}{\mathrm{LAI}/\mathrm{LAI}_{\mathrm{thr}}} - 1\right)$ (Leung et al., 2023; Okin, 2008).

The wet fluid threshold velocity u_{*ft} is calculated using Equation (A4), except the dry fluid threshold velocity u_{*ft0} is calculated by (Shao and Lu, 2000):

$$u_{*ft0} = \sqrt{A\left(\rho_p g D_p + \gamma/D_p\right)/\rho_a} \tag{A19}$$

where A = 0.0123 and $\gamma = 1.65 \times 10^{-4}$ kg s^{-2} are empirical constants (Darmenova et al., 2009; Leung et al., 2023); $D_p = 127 \pm 47$ μm is the median diameter of soil particle as evaluated from various field measurements in Leung et al. (2023).

Once the saltation is initialized, the threshold velocity required to maintain the saltation

795 diminishes, which is defined as the dynamic or impact threshold friction velocity u_{*it} in m s^{-1}
796 (Martin and Kok, 2018):

797 $$u_{*it} = B_{it} u_{*ft0} \tag{A20}$$

798 where $B_{it} = 0.82$. A prior study suggested that the impact threshold primarily governed the
799 saltation flux (Martin and Kok, 2018) and thus u_{*it} is adopted as the governing threshold in Equation
800 (14).

801 The standardized wet fluid threshold friction velocity u_{*st} was proposed and argued as a central
802 factor to characterize soil aridity by a prior study (Kok et al., 2014):

803 $$u_{*st} = u_{*ft} \sqrt{\rho_a / \rho_{a0}} \tag{A21}$$

804 where $\rho_{a0} = 1.225\ \mathrm{kg\ m^{-3}}$ is the standard surface air density.

805 The fragmentation exponent of κ quantifies the sensitivity of F_d to u_{*s} and is capped at 3 to prevent
806 excessive sensitivity of the model to wind speeds according to (Kok et al., 2014; Leung et al., 2024):

807 $$\kappa = C_\kappa \frac{(u_{*st} - u_{*st0})}{u_{*st0}} \tag{A22}$$

808 where $C_\kappa = 2.7 \pm 1.0$ and $u_{*st0} = 0.16\ \mathrm{m\ s^{-1}}$ are constants.

809 The time-varying soil erodibility coefficient is a function of u_{*st} only (Kok et al., 2014):

810 $$C_d = C_{d0} \exp\left(-C_e \frac{u_{*st} - u_{*st0}}{u_{*st0}}\right) \tag{A23}$$

811 where $C_{d0} = (4.4 \pm 0.5) \times 10^{-5}$ and $C_e = 2.0 \pm 0.3$ are empirical constants.

812

Table A1. The mean and standard deviation (σ) of surface $PM_{2.5}$ dust measured from 25 SPARTAN sites with at least 10 samples in 5 years from 2019 to 2023 globally. Sites are sorted by the mean surface $PM_{2.5}$ dust concentrations.

Site	# of samples	Sampling days[a]	Sampling seasons	Start date for MAIA sites	Mean ($\mu g\ m^{-3}$)	σ ($\mu g\ m^{-3}$)
Abu Dhabi	113	1012	MAM, JJA, SON, DJF	-	13.4	6.7
Ilorin	47	411	MAM, JJA, SON, DJF	-	11.2	15.6
Kanpur	15	135	MAM, JJA, SON, DJF	-	8.2	7.3
Dhaka	49	170	MAM, JJA, SON	-	6.8	3.5
Addis Ababa	117	234	MAM, JJA, SON, DJF	12/7/2022	4.9	1.6
Beijing	83	424	MAM, JJA, SON, DJF	8/30/2022	4.2	2.0
Rehovot	181	571	MAM, JJA, SON, DJF	11/5/2021	4.2	4.0
Haifa	142	284	MAM, JJA, SON, DJF	2/16/2022	3.3	3.4
Seoul	83	744	MAM, JJA, SON, DJF	-	2.5	1.5
Fajardo	52	453	MAM, JJA, SON, DJF	-	2.3	2.3
Bujumbura	19	171	MAM, JJA, SON, DJF	-	2.0	1.2
Kaohsiung	122	244	MAM, JJA, SON, DJF	8/20/2022	1.9	0.8
Ulsan	77	682	MAM, JJA, SON, DJF	-	1.9	1.3
Pretoria	223	450	JJA, SON	4/15/2021	1.7	0.6
Bandung	28	249	MAM, JJA, SON, DJF	-	1.7	0.5
Singapore	13	117	JJA, SON, DJF	-	1.3	0.4
Johannesburg	166	331	MAM, JJA, SON, DJF	4/7/2022	1.3	0.3
Mexico City	49	425	MAM, JJA, SON, DJF	-	1.3	0.5
Taipei	211	421	MAM, JJA, SON, DJF	1/27/2022	1.1	0.9
Pasadena	242	484	MAM, JJA, SON, DJF	11/9/2021	0.8	0.3
Lethbridge	13	121	MAM, JJA, SON, DJF	-	0.7	0.3
Melbourne	34	307	MAM, JJA	-	0.6	0.8
Downsview	18	144	MAM, JJA, SON, DJF	-	0.5	0.2
Sherbrooke	83	687	MAM, JJA, DJF	-	0.4	0.2
Halifax	116	801	MAM, JJA, SON, DJF	-	0.3	0.1

[a]The number of days when SPARTAN sampling occurred for a part of the day according to either the standard 9-day protocol or the MAIA protocol.

819 Table A2. The values of a global tuning factor C_{tune} used for different simulations.

Simulation	C_{tune}
Emis*	
Emis	2.358×10^{-2}
EmisClay	2.569×10^{-3}
EmisClayWet	2.146×10^{-3}
EmisClayWetLAI$_{thr}$	2.170×10^{-3}
Emis*PSD	2.945×10^{-3}
Emis*PSD7Bins0.5AD	2.892×10^{-3}
Emis*PSD7Bins0.5ADWetDep	2.832×10^{-3}

820

821 Table A3. Effects of different modifications on the model performance of simulated annual surface
822 $PM_{2.5}$ dust versus SPARTAN over sites with >50 samples in terms of the correlation coefficient (*r*),
823 the reduced-major-axis linear regression slope, and the normalized mean difference (NMD).

Simulation	Simulated surface $PM_{2.5}$ dust versus SPARTAN		
	r	slope	NMD (%)
Base	0.96	2.71	115.8
Emis*			
Emis	0.97	2.24	87.1
EmisClay	0.97	2.01	45.7
EmisClayWet	0.97	2.30	89.8
EmisClayWetLAI$_{thr}$	0.97	2.23	78.7
Emis*PSD	0.97	1.90	53.1
Emis*PSD7Bins0.5AD	0.96	1.85	64.6
Emis*PSD7Bins0.5ADWetDep	0.97	1.80	58.2

824

825

826 Table A4. Computational demand of 4-bin and 7-bin dust simulations

Type	Number of physical cores (CPUs)[a]	Throughput (d d^{-1})
4 dust bins	108	78.9
7 dust bins		74.2

827 [a]Calculated on Intel® Xeon® Gold 6154 with the clock speed of 3.00 GHz.

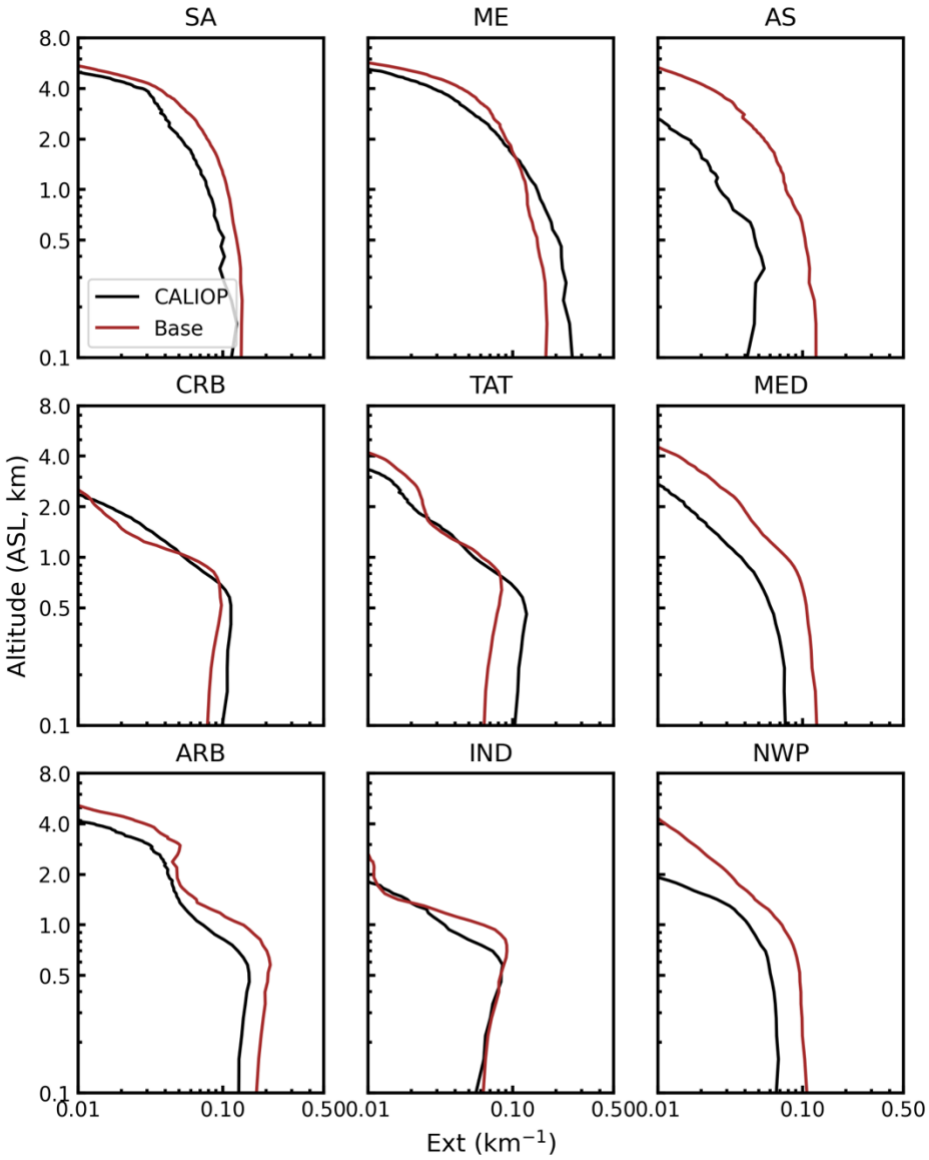

828

829 Figure A1. Same as Figure 3 but for the absolute extinction vertical profile.

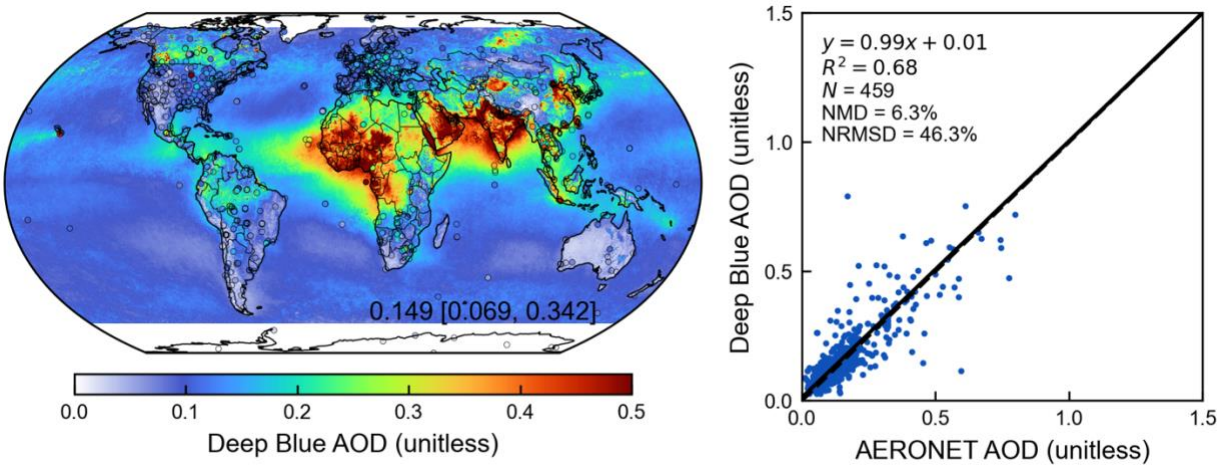

Figure A2. Annual aerosol optical depth (AOD) from the Deep Blue satellite retrieval and comparison against ground-based observations from AERONET in the year of 2018. Filled circles on the map represent ground-based observations from AERONET. Inset values at the bottom right of the map are arithmetical mean with 5th and 95th percentiles in the square brackets. Regression statistics including the reduced-major-axis linear regression equation, coefficient of variation (R^2), total number of points (N), normalized mean difference (NMD), and normalized root-mean-square difference (NRMSD) are listed at the top left of the scatter plot.

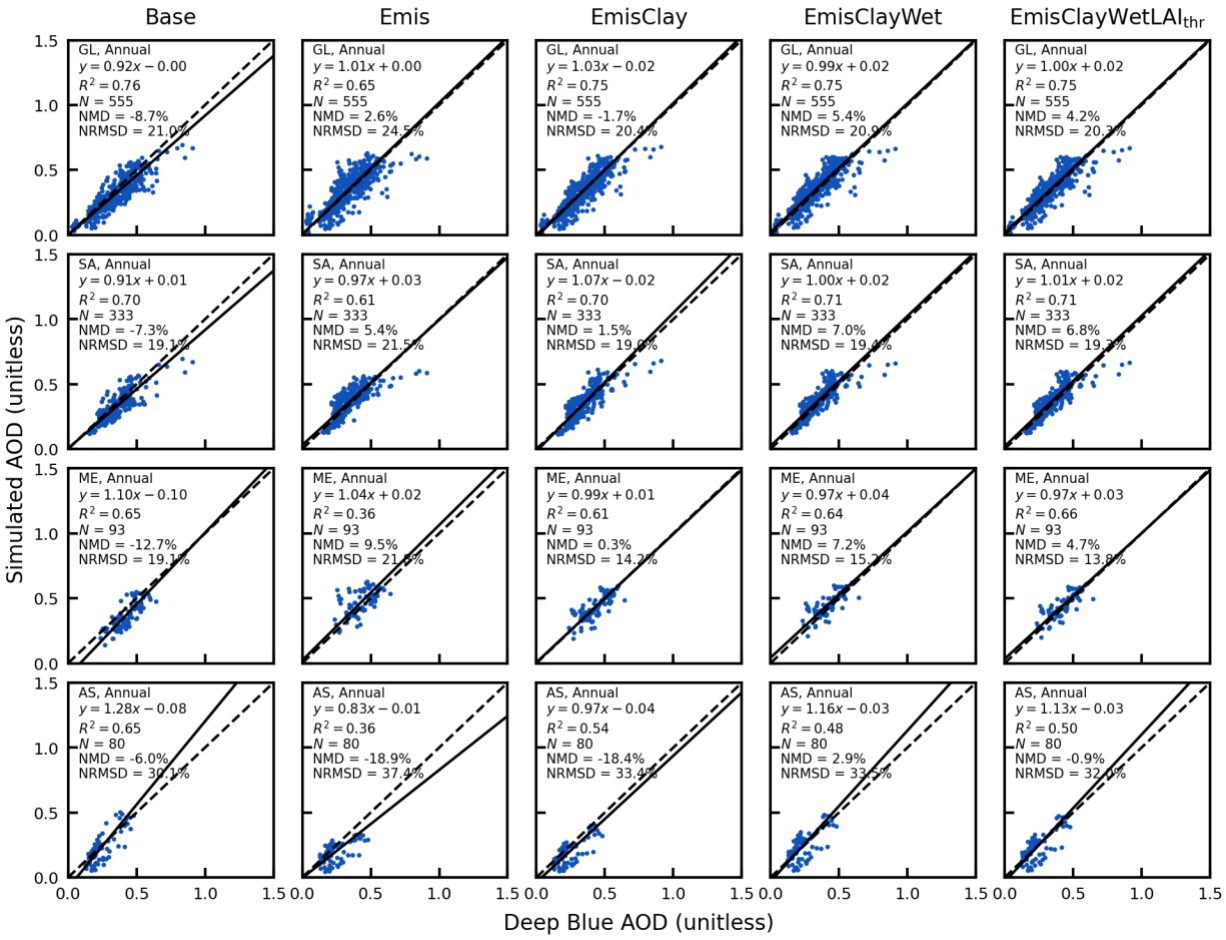

838

839 Figure A3. Same as Figure 6 but over the same dust source regions for the Base scheme for all dust

840 emission scheme comparisons versus Deep Blue AOD.

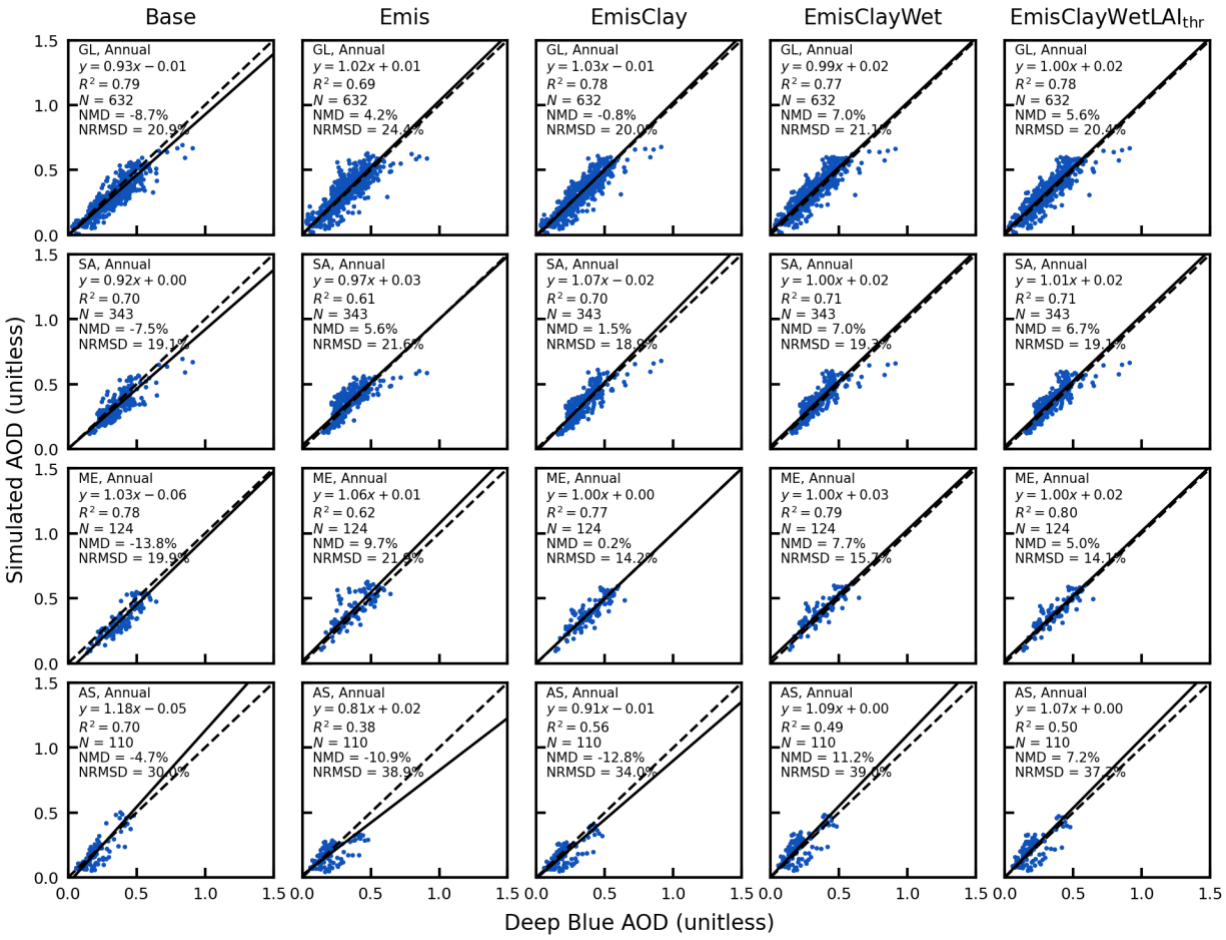

841

842 Figure A4. Same as Figure 6 but over the same dust source regions for the EmisClayWetLAI$_{thr}$

843 scheme for all dust emission scheme comparisons versus Deep Blue AOD.

844

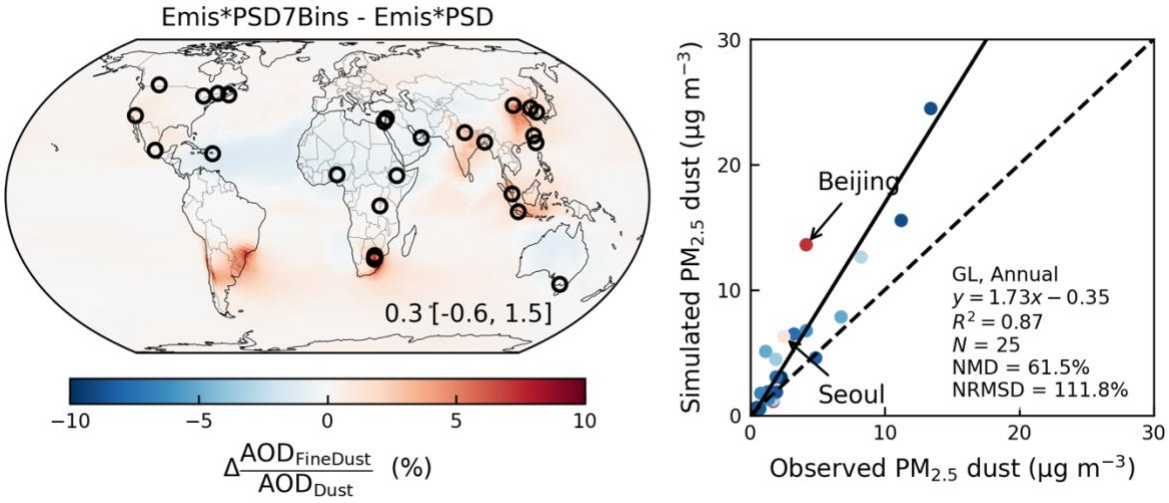

Figure A5. Differences of the fractional contributions of fine dust with geometric diameter less than 2 μm to total dust column abundance ($\mathrm{AOD_{FineDust}}/\mathrm{AOD_{Dust}}$) between the Emis*PSD7Bins and Emis*PSD simulations (left); Comparison between simulated $PM_{2.5}$ dust against SPARTAN measurements from the Emis*PSD7Bins simulation with color coded by the differences of $\mathrm{AOD_{FineDust}}/\mathrm{AOD_{Dust}}$ between the Emis*PSD7Bins and Emis*PSD simulations over SPARTAN sites. Open circles in the map indicate SPARTAN sites. Inset values at the bottom right of the map are arithmetical mean with 5th and 95th percentiles in the square brackets. Regression statistics including the reduced-major-axis linear regression equation, coefficient of variation (R^2), total number of points (N), normalized mean difference (NMD), and normalized root-mean-square difference (NRMSD) are listed at the bottom right of the scatter plot.

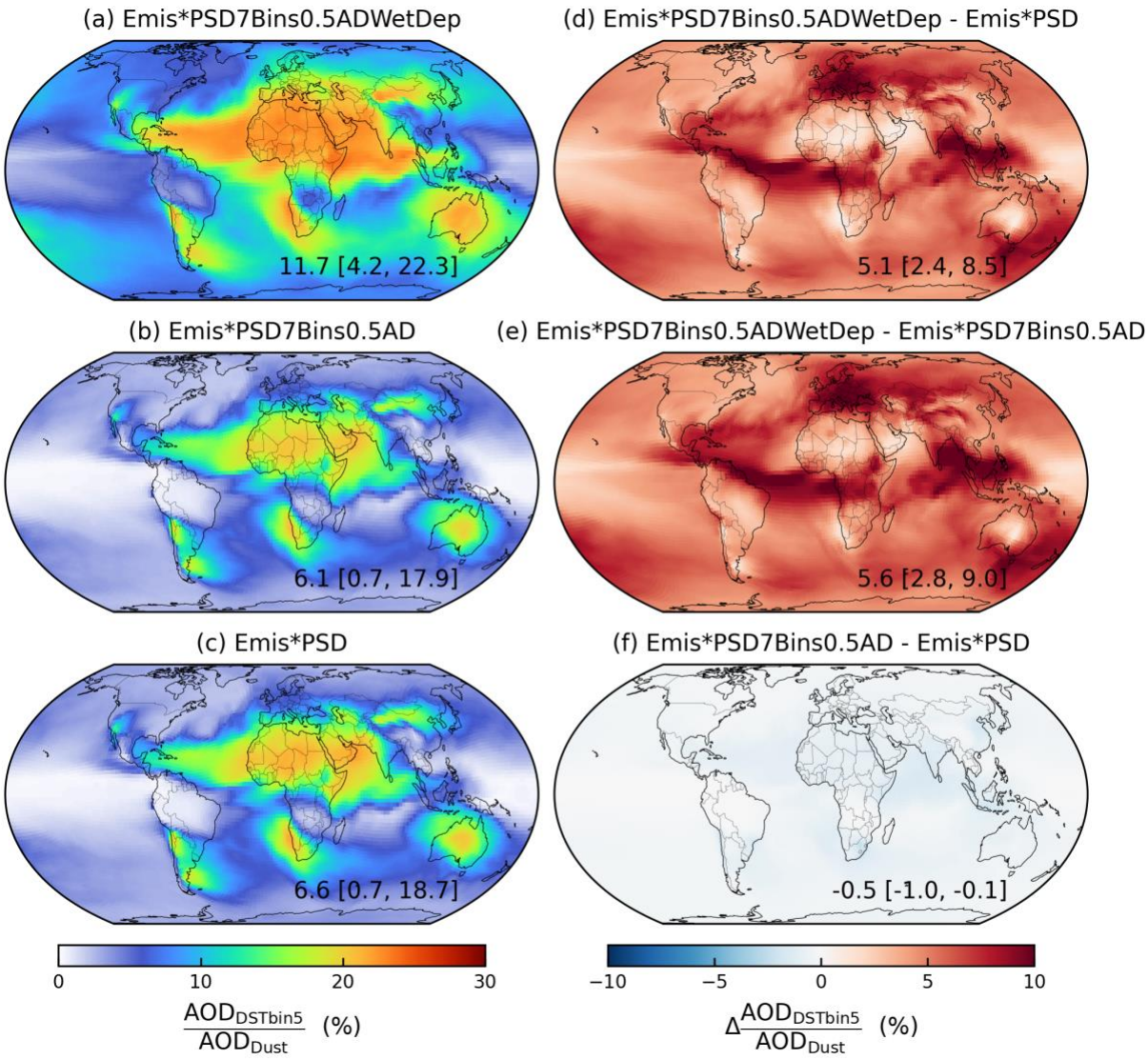

856

857 Figure A6. Fractional contributions of DSTbin5 to total dust column abundance
858 ($\mathrm{AOD_{DSTbin5}}/\mathrm{AOD_{Dust}}$) from the a) Emis*PSD7Bins0.5ADWetDep, b) Emis*PSD7Bins0.5AD, c)
859 Emis*PSD and their absolute differences. Inset values at the bottom right are arithmetical mean
860 with 5th and 95th percentiles in the square brackets.

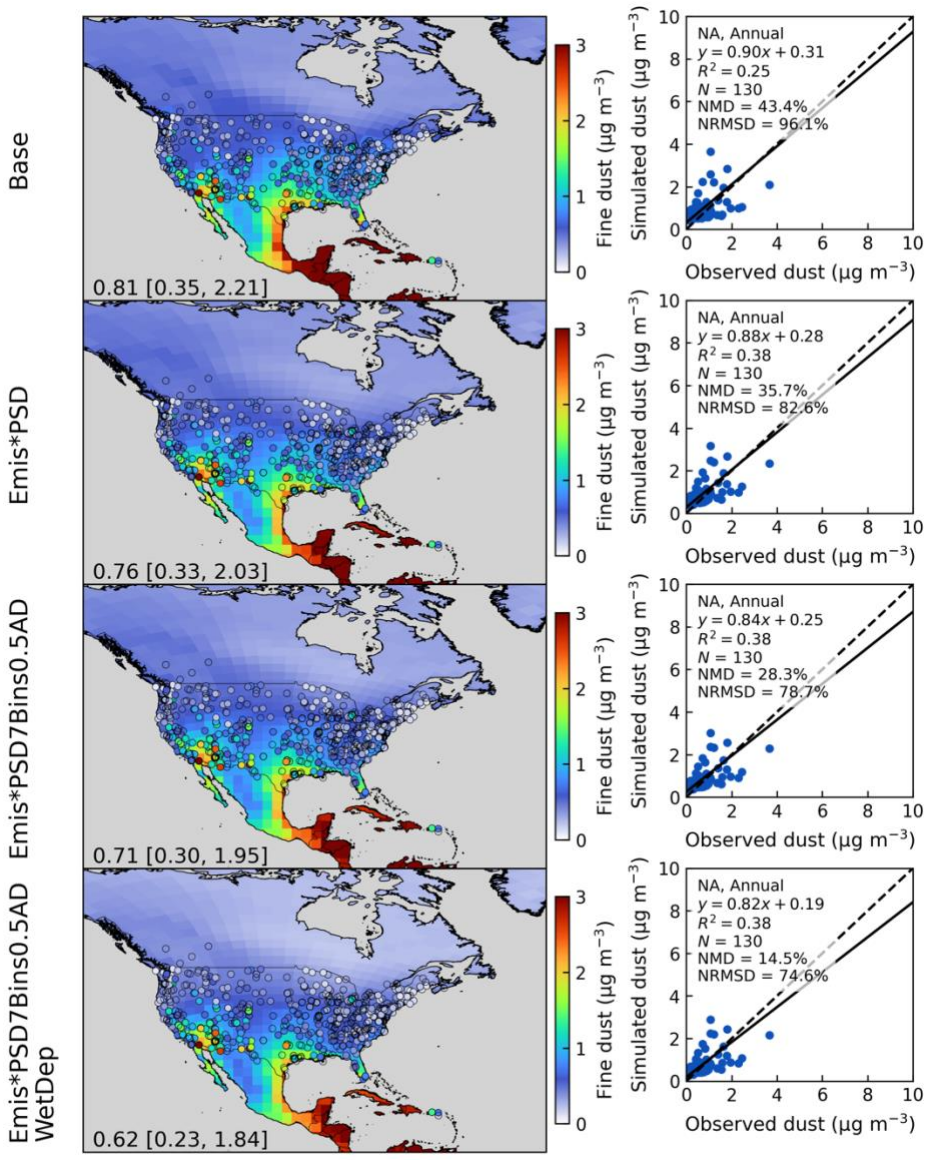

Figure A7. Comparisons of simulated annual surface $PM_{2.5}$ dust against ground-based observations in the year of 2018 over North America from the Base (top), Emis*PSD (second), Emis*PSD7Bins0.5AD (third), and Emis*PSD7Bins0.5ADWetDep (bottom) simulations. Filled circles represent ground-based observations of surface $PM_{2.5}$ dust concentrations. Inset values at the bottom left are arithmetical mean with 5th and 95th percentiles in the square brackets. Regression statistics including the reduced-major axis linear regression equation, coefficient of variation (R^2), total number of points (N), normalized mean difference (NMD), and normalized root-mean-square difference (NRMSD) are listed at the top left of right panels.

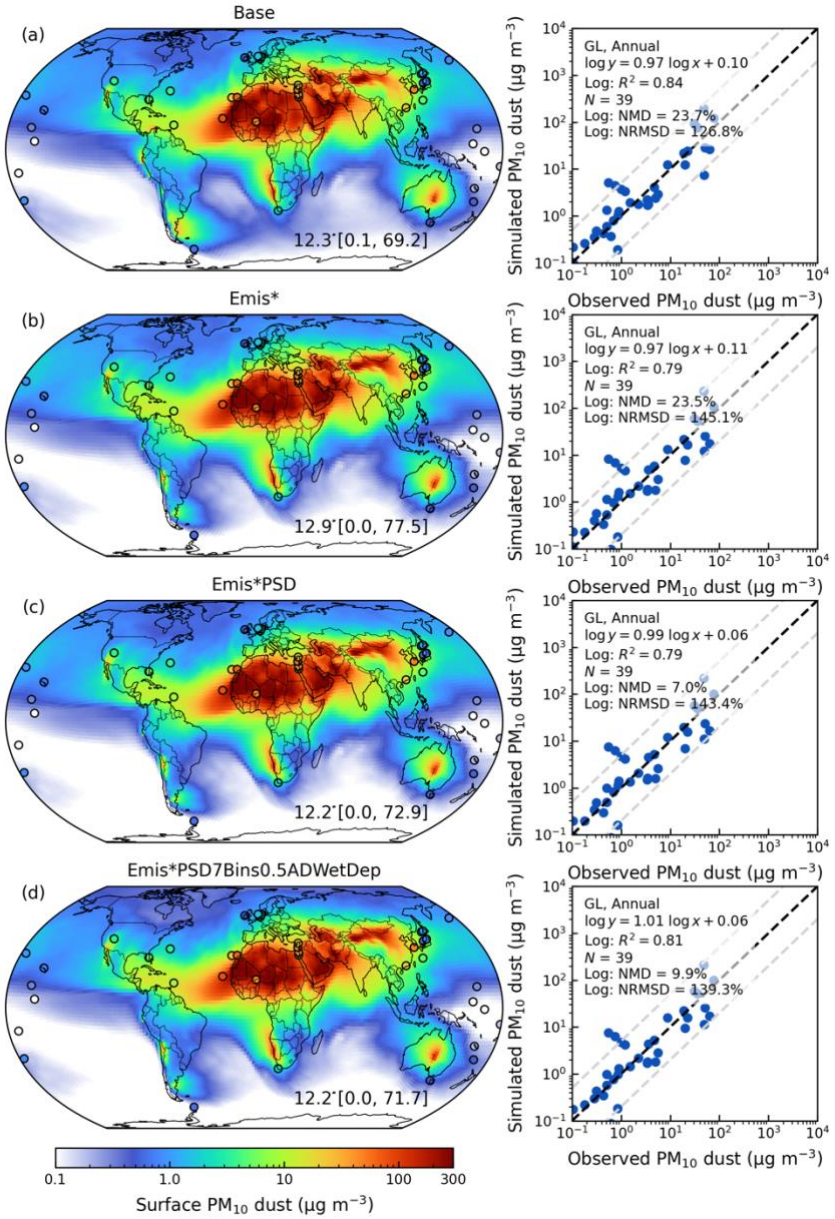

870

871 Figure A8. Annual simulated surface PM_{10} dust concentrations in the year of 2018 from the
872 simulations of a) Base, b) Emis*, c) Emis*PSD, and d) Emis*PSD7Bins0.5ADWetDep. Filled circles
873 represent ground-based observations of surface PM_{10} dust concentrations. Inset values at the
874 bottom right are arithmetical mean with 5th and 95th percentiles in the square brackets. Dash lines
875 in the scatter plots indicate variations within a factor of 5. Regression statistics including the
876 reduced-major-axis linear regression equation, coefficient of variation (R^2), total number of points
877 (N), normalized mean difference (NMD), and normalized root-mean-square difference (NRMSD) are
878 listed at the top left of right panels.

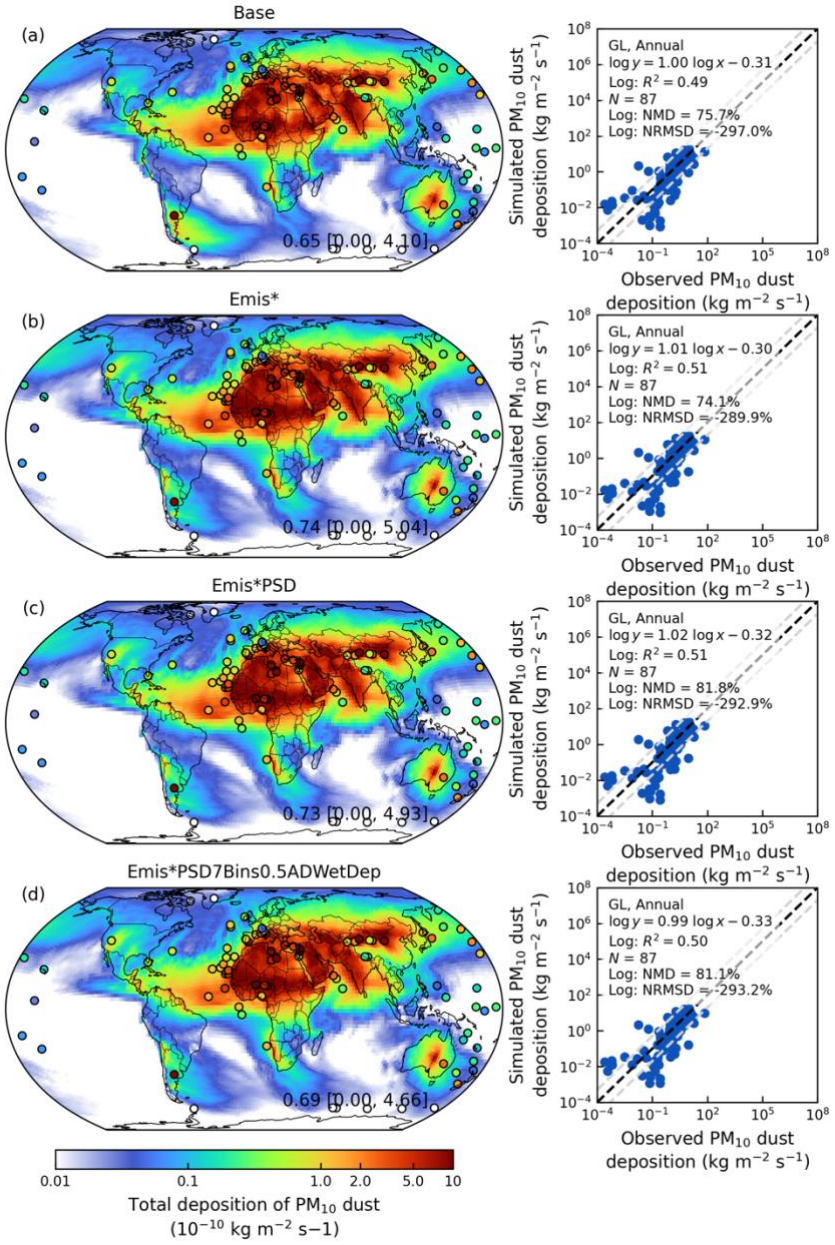

879

880 Figure A9. Annual simulated total deposition of PM_{10} dust within the troposphere in the year of 2018
881 from the simulations of a) Base, b) Emis*, c) Emis*PSD, and d) Emis*PSD7Bins0.5ADWetDep.
882 Filled circles represent ground-based observations of surface PM_{10} dust deposition. Inset values at
883 the bottom right are arithmetical mean with 5th and 95th percentiles in the square brackets. Dash
884 lines in the scatter plots indicate variations within a factor of 5. Regression statistics including the
885 reduced-major-axis linear regression equation, coefficient of variation (R^2), total number of points
886 (N), normalized mean difference (NMD), and normalized root-mean-square difference (NRMSD) are
887 listed at the top left of right panels.

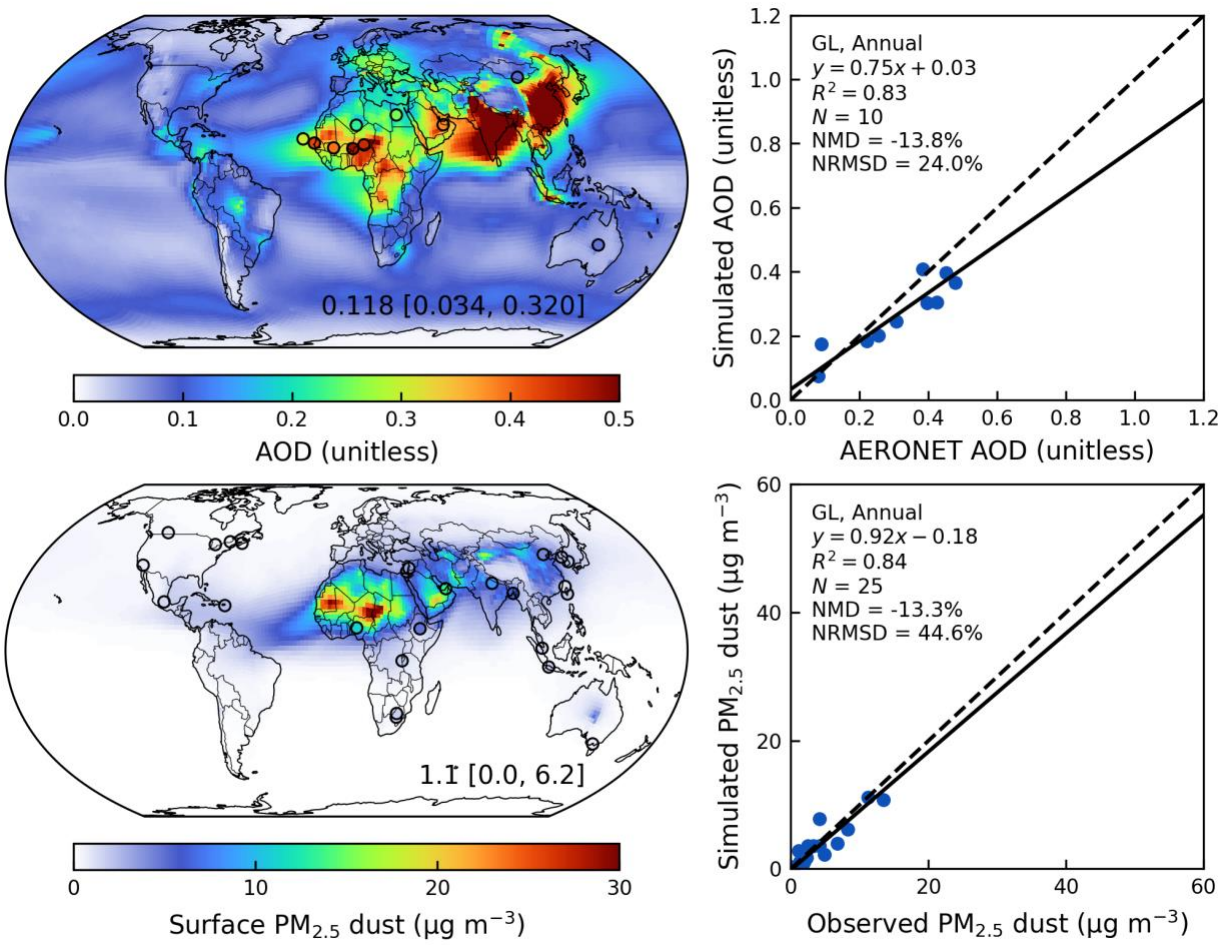

888

889 Figure A10. Annual simulated aerosol optical depth (AOD) and comparison against ground-based
890 observations from AERONET over dusty regions ($\mathrm{AOD_{Dust}/AOD} > 0.5$) (top); Annual simulated
891 surface $PM_{2.5}$ dust and comparison against ground-based measurements from SPARTAN from the
892 Emis*PSD7Bins0.5ADWetDep simulation with the dust emissions calculated at C48 resolution in
893 the year of 2018 (bottom). Filled circles on the maps represent ground-based observations from
894 SPARTAN and AERONET. Inset values at the bottom right of the maps are arithmetical mean with
895 5th and 95th percentiles in the square brackets. Regression statistics including the reduced-major-
896 axis linear regression equation, coefficient of variation (R^2), total number of points (N), normalized
897 mean difference (NMD), and normalized root-mean-square difference (NRMSD) are listed at the
898 top left of the scatter plots.

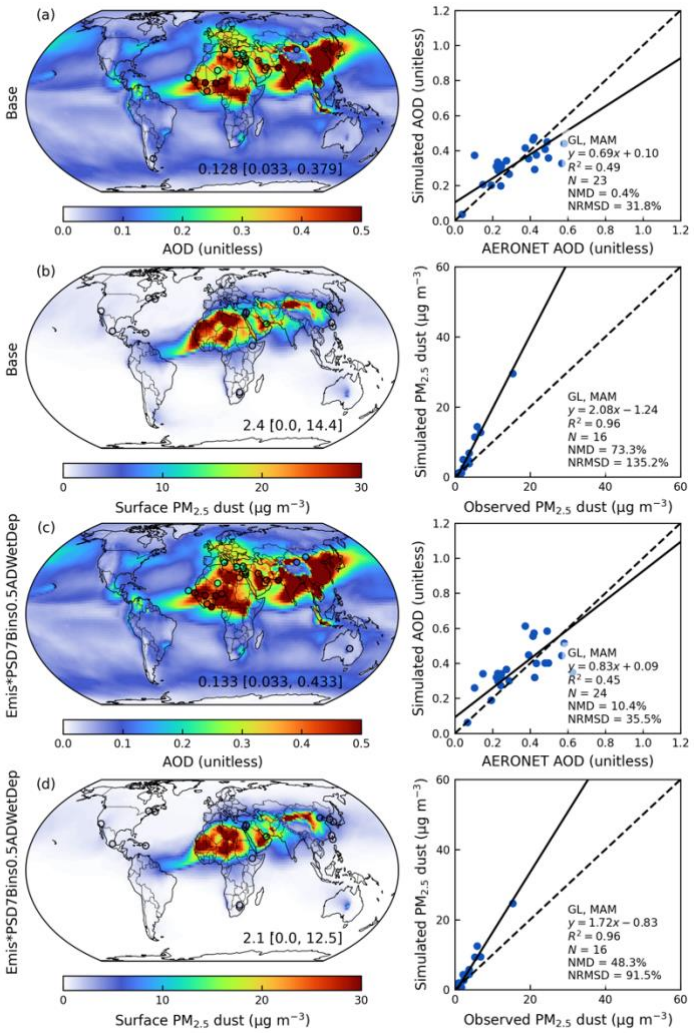

Figure A11. Simulated seasonal mean (March, April, and May or MAM) aerosol optical depth (AOD; a and c) and surface $PM_{2.5}$ dust (b and d) from the Base and Emis*PSD7Bins0.5ADWetDep simulations. Filled circles on the maps represent ground-based observations from SPARTAN and AERONET. Inset values at the bottom right of the maps are arithmetical mean with 5th and 95th percentiles in the square brackets. Comparisons of simulated AOD versus AERONET AOD over dusty sites ($\mathrm{AOD_{Dust}}/\mathrm{AOD} > 0.5$), and simulated surface $PM_{2.5}$ dust versus SPARTAN observations are shown in the right panels. Regression statistics including the reduced-major-axis linear regression equation, coefficient of variation (R^2), total number of points (N), normalized mean difference (NMD), and normalized root-mean-square difference (NRMSD) are listed at the bottom right of the scatter plots.

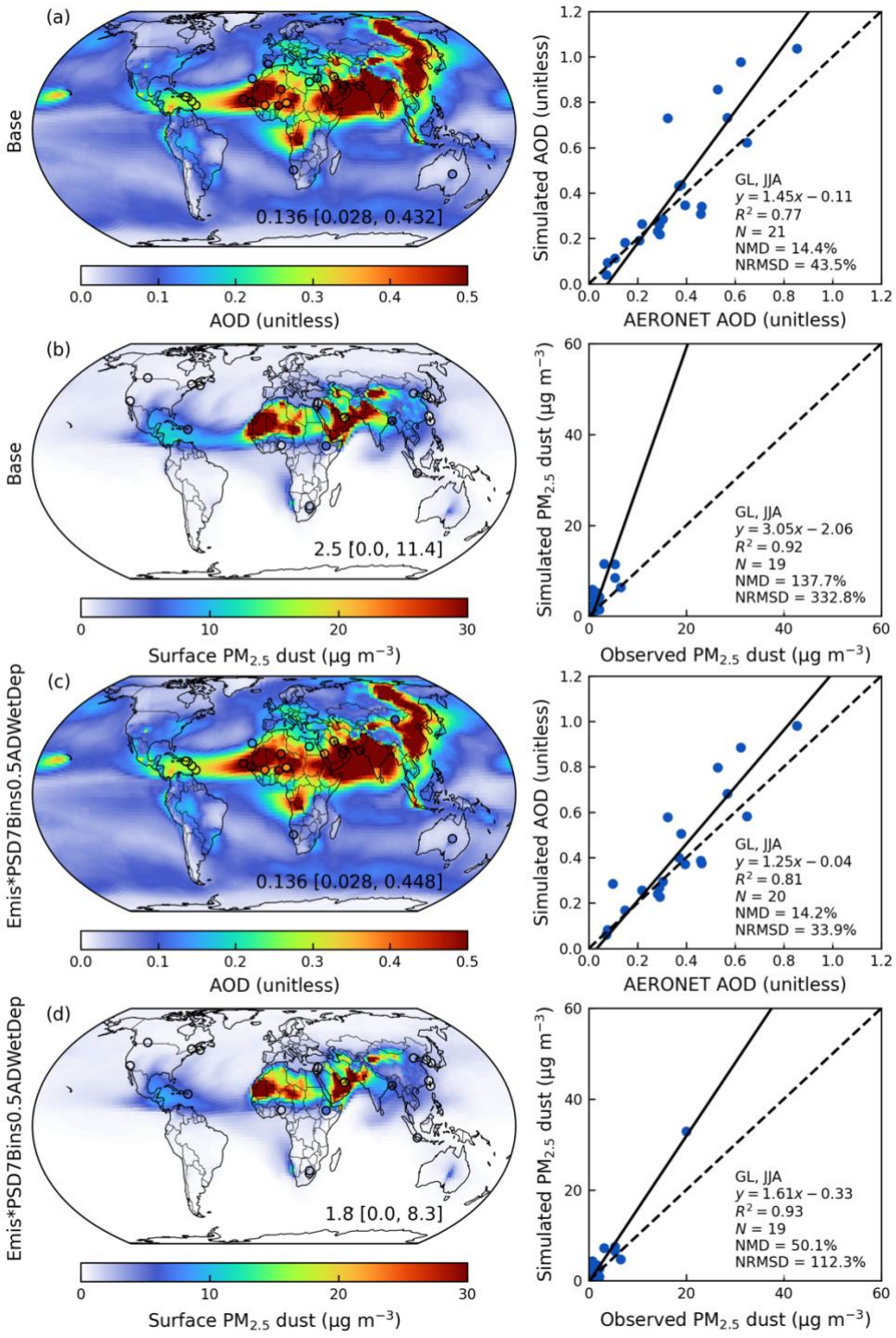

910

911 Figure A12. Same as Figure A11 but for the seasonal mean of June, July, and August (JJA).

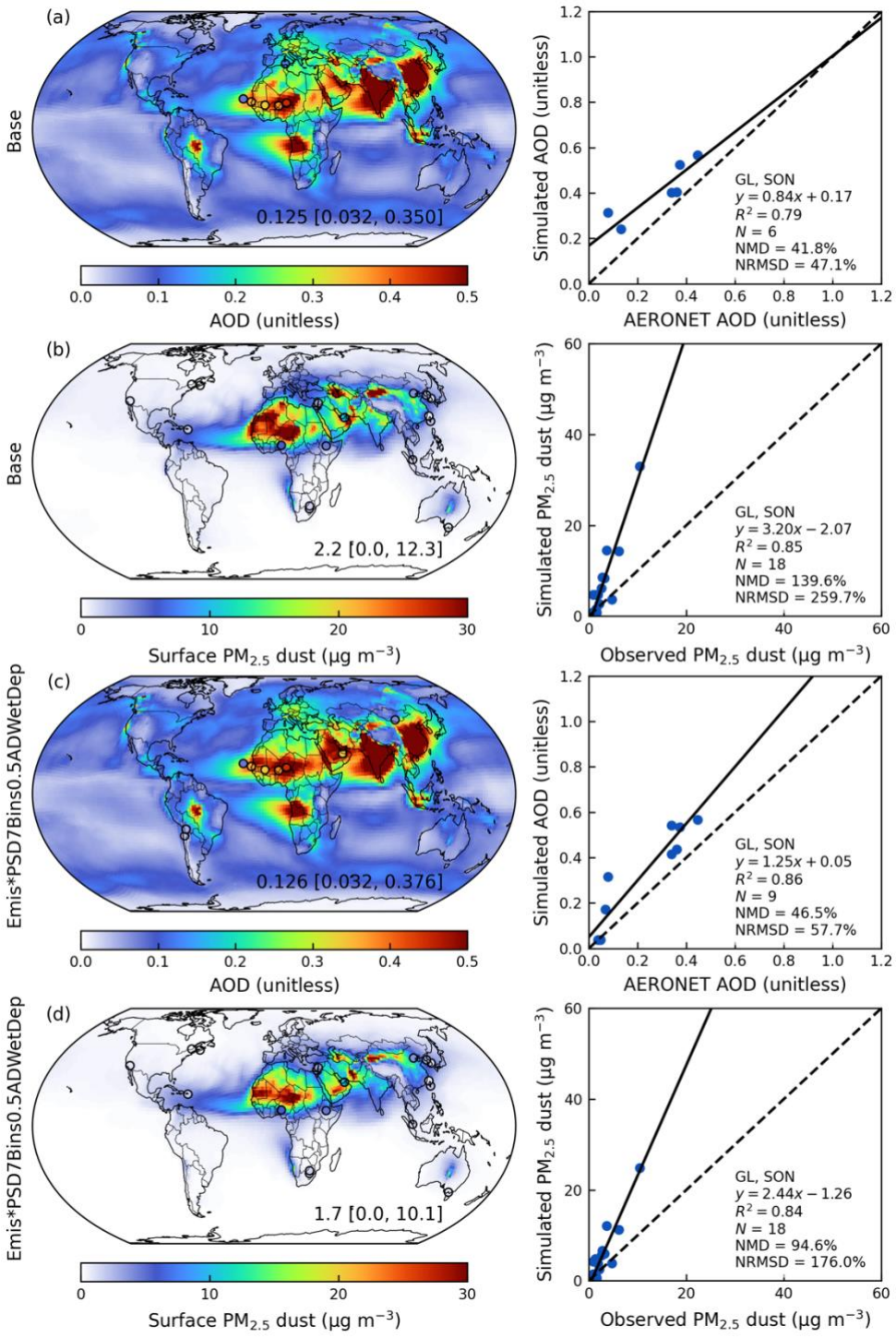

912

913 Figure A13. Same as Figure A11 but for the seasonal mean of September, October, and November
914 (SON).

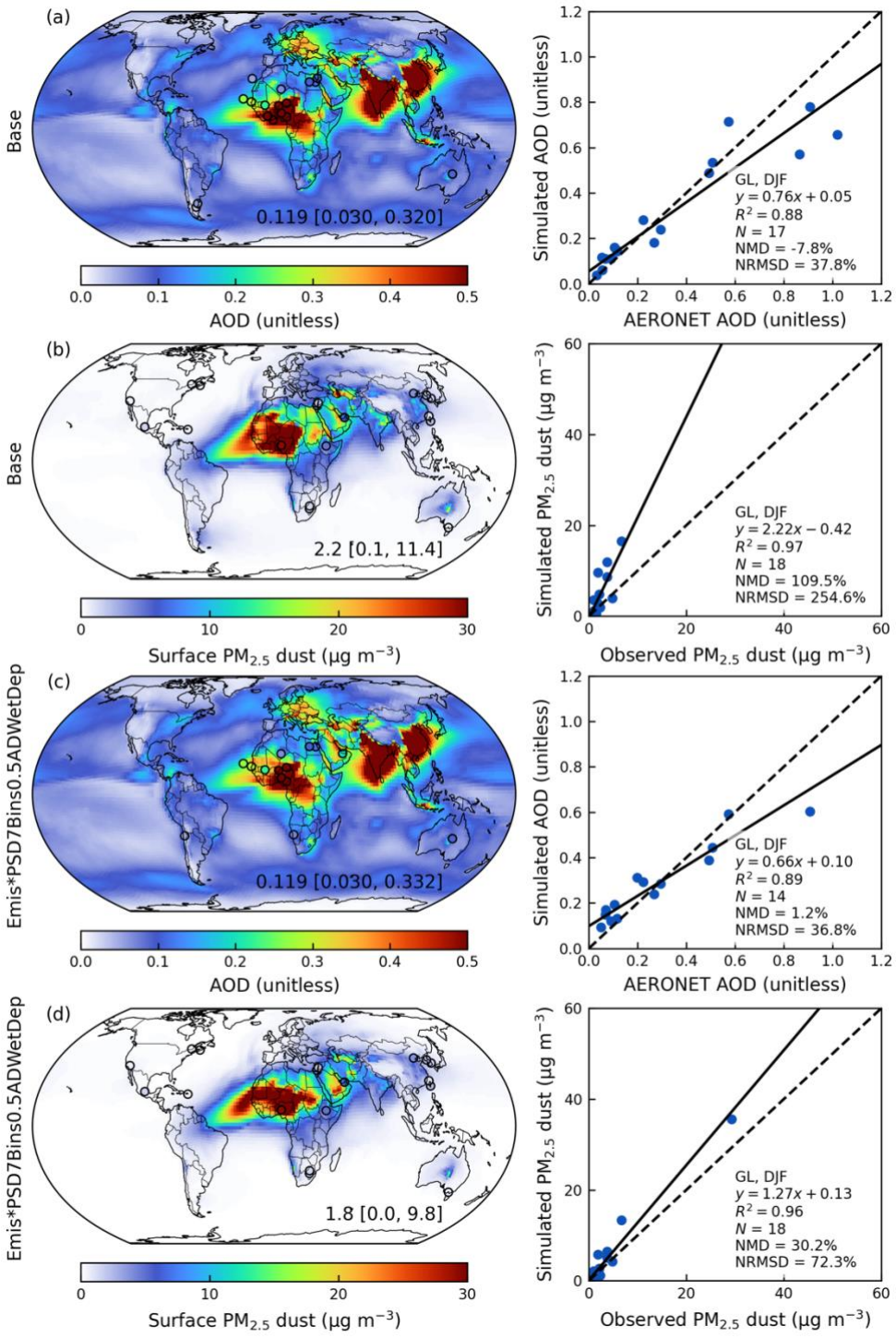

915

916 Figure A14. Same as Figure A11 but for the seasonal mean of December, January, and February
917 (DJF).

Code availability. The standard GEOS-Chem in its high-performance configuration version 14.4.1 can be downloaded at https://doi.org/10.5281/zenodo.12584305 (The International GEOS-Chem User Community, 2024). The model source code, an example run directory, and the calculation scripts for the hourly dust emission fluxes for the revised simulation can be downloaded at https://doi.org/10.5281/zenodo.14510793 (Zhang, 2024).

Data availability. The surface $PM_{2.5}$ dust measurements with the attenuation correction from SPARTAN used in this study are publicly available at https://www.spartan-network.org/data (last access: 18 March 2025). The PM_{10} dust and total deposition of dust are available at https://doi.org/10.5281/zenodo.6989502 (Li et al., 2022a). The processed meteorological fields from GEOS-FP are available at http://geoschemdata.wustl.edu/ExtData/GEOS_0.25x0.3125/GEOS_FP/ (last access: 4 February 2025) with the soil porosity downloaded from the constant land-surface parameter of MERRA2 M2C0NXLND collection (https://disc.gsfc.nasa.gov/datasets?project=MERRA-2, last access: 4 February 2025). The land cover dataset can be downloaded at https://lpdaac.usgs.gov/products/mcd12c1v061/ (last access: 4 February 2025). The monthly mean leaf area index at 0.5 degree can be downloaded at http://globalchange.bnu.edu.cn/research/laiv6 (last access: 4 February 2025). The satellite-derived aeolian roughness data are available upon contacting Catherine Prigent. The GSDE soil dataset can be downloaded at http://globalchange.bnu.edu.cn/research/soilw (last access: 4 February 2025).

Author contribution. The manuscript was written by DZ and RVM with contributions from all authors. DZ and RVM designed the study with developments of the methodology. DZ conducted simulations and analyzed the results. XL developed the methodology for the mineral dust concentration construction in SPARTAN. AvD compiled the Deep Blue AOD dataset and ground-based observation datasets of surface $PM_{2.5}$ dust over NA and AERONET AOD for evaluation. XL, CRO and EW contributed to SPARTAN measurements. YL contributed to the dry deposition analysis. JM offered valuable discussion for the emission scheme refinements. DML and JFK contributed to the development of a new dust emission scheme. LL constructed the observational data for PM_{10} dust and deposition flux. HZ contributed to the generation of SPARTAN dust data. JRT and YY contributed to the discussion of the evaluation of simulated dust. MB and YR contributed to the establishment and maintenance of SPARTAN monitoring sites. All authors contributed to

revising the manuscript.

Competing interests. The authors declare no competing financial interest.

Acknowledgements. This work was supported by the National Science Foundation grants 2244984 and 2151093, and the National Aeronautics and Space Administration grant 80NSSC22K0200. The GEOS-FP data used in this study have been provided by the Global Modeling and Assimilation Office (GMAO) at the NASA Goddard Space Flight Center. We thank the AERONET, CALIOP, MODIS, and VIIRS teams for the creation and public release of their data products.

References

Amato, F., Schaap, M., Denier van der Gon, H. A. C., Pandolfi, M., Alastuey, A., Keuken, M., and Querol, X.: Short-term variability of mineral dust, metals and carbon emission from road dust resuspension, Atmospheric Environment, 74, 134–140, https://doi.org/10.1016/j.atmosenv.2013.03.037, 2013.

Bagheri, G. and Bonadonna, C.: On the drag of freely falling non-spherical particles, Powder Technology, 301, 526–544, https://doi.org/10.1016/j.powtec.2016.06.015, 2016.

Bayon, G., Garzanti, E., Dinis, P., Beaufort, D., Barrat, J.-A., Germain, Y., Trinquier, A., Barbarano, M., Overare, B., Adeaga, O., and Braquet, N.: Contribution of Saharan dust to chemical weathering fluxes and associated phosphate release in West Africa, Earth and Planetary Science Letters, 641, 118845, https://doi.org/10.1016/j.epsl.2024.118845, 2024.

Bey, I., Jacob, D. J., Yantosca, R. M., Logan, J. A., Field, B. D., Fiore, A. M., Li, Q., Liu, H. Y., Mickley, L. J., and Schultz, M. G.: Global modeling of tropospheric chemistry with assimilated meteorology: Model description and evaluation, Journal of Geophysical Research: Atmospheres, 106, 23073–23095, https://doi.org/10.1029/2001JD000807, 2001.

Bouwman, A. F., Lee, D. S., Asman, W. A. H., Dentener, F. J., Van Der Hoek, K. W., and Olivier, J. G. J.: A global high-resolution emission inventory for ammonia, Global Biogeochemical Cycles, 11, 561–587, https://doi.org/10.1029/97GB02266, 1997.

Breider, T. J., Mickley, L. J., Jacob, D. J., Ge, C., Wang, J., Payer Sulprizio, M., Croft, B., Ridley, D. A., McConnell, J. R., Sharma, S., Husain, L., Dutkiewicz, V. A., Eleftheriadis, K., Skov, H., and Hopke, P. K.: Multidecadal trends in aerosol radiative forcing over the Arctic: Contribution of changes in

977 anthropogenic aerosol to Arctic warming since 1980, Journal of Geophysical Research:
978 Atmospheres, 122, 3573–3594, https://doi.org/10.1002/2016JD025321, 2017.

979 Cakmur, R. V., Miller, R. L., Perlwitz, J., Geogdzhayev, I. V., Ginoux, P., Koch, D., Kohfeld, K. E.,
980 Tegen, I., and Zender, C. S.: Constraining the magnitude of the global dust cycle by minimizing the
981 difference between a model and observations, Journal of Geophysical Research: Atmospheres,
982 111, https://doi.org/10.1029/2005JD005791, 2006.

983 Cao, C., De Luccia, F. J., Xiong, X., Wolfe, R., and Weng, F.: Early On-Orbit Performance of the
984 Visible Infrared Imaging Radiometer Suite Onboard the Suomi National Polar-Orbiting Partnership
985 (S-NPP) Satellite, IEEE Transactions on Geoscience and Remote Sensing, 52, 1142–1156,
986 https://doi.org/10.1109/TGRS.2013.2247768, 2014.

987 Comola, F., Kok, J. F., Chamecki, M., and Martin, R. L.: The Intermittency of Wind-Driven Sand
988 Transport, Geophysical Research Letters, 46, 13430–13440,
989 https://doi.org/10.1029/2019GL085739, 2019.

990 Croft, B., Wentworth, G. R., Martin, R. V., Leaitch, W. R., Murphy, J. G., Murphy, B. N., Kodros, J. K.,
991 Abbatt, J. P. D., and Pierce, J. R.: Contribution of Arctic seabird-colony ammonia to atmospheric
992 particles and cloud-albedo radiative effect, Nature Communications, 7, 13444,
993 https://doi.org/10.1038/ncomms13444, 2016.

994 Darmenova, K., Sokolik, I. N., Shao, Y., Marticorena, B., and Bergametti, G.: Development of a
995 physically based dust emission module within the Weather Research and Forecasting (WRF)
996 model: Assessment of dust emission parameterizations and input parameters for source regions in
997 Central and East Asia, Journal of Geophysical Research: Atmospheres, 114, D14201,
998 https://doi.org/10.1029/2008JD011236, 2009.

999 Eastham, S. D., Long, M. S., Keller, C. A., Lundgren, E., Yantosca, R. M., Zhuang, J. W., Li, C., Lee, C.
1000 J., Yannetti, M., Auer, B. M., Clune, T. L., Kouatchou, J., Putman, W. M., Thompson, M. A., Trayanov,
1001 A. L., Molod, A. M., Martin, R. V., and Jacob, D. J.: GEOS-Chem High Performance (GCHP v11-02c):
1002 a next-generation implementation of the GEOS-Chem chemical transport model for massively
1003 parallel applications, Geoscientific Model Development, 11, 2941–2953,
1004 https://doi.org/10.5194/gmd-11-2941-2018, 2018.

1005 Emerson, E. W., Hodshire, A. L., DeBolt, H. M., Bilsback, K. R., Pierce, J. R., McMeeking, G. R., and

Farmer, D. K.: Revisiting particle dry deposition and its role in radiative effect estimates, Proceedings of the National Academy of Sciences, 117, 26076–26082, https://doi.org/10.1073/pnas.2014761117, 2020.

Fairlie, T. D., Jacob, D. J., and Park, R. J.: The impact of transpacific transport of mineral dust in the United States, Atmospheric Environment, 41, 1251–1266, https://doi.org/10.1016/j.atmosenv.2006.09.048, 2007.

Fécan, F., Marticorena, B., and Bergametti, G.: Parametrization of the increase of the aeolian erosion threshold wind friction velocity due to soil moisture for arid and semi-arid areas, Annales Geophysicae, 17, 149–157, https://doi.org/10.1007/s00585-999-0149-7, 1999.

Feng, L., Smith, S. J., Braun, C., Crippa, M., Gidden, M. J., Hoesly, R., Klimont, Z., van Marle, M., van den Berg, M., and van der Werf, G. R.: The generation of gridded emissions data for CMIP6, Geoscientific Model Development, 13, 461–482, https://doi.org/10.5194/gmd-13-461-2020, 2020.

Fisher, J. A., Jacob, D. J., Wang, Q., Bahreini, R., Carouge, C. C., Cubison, M. J., Dibb, J. E., Diehl, T., Jimenez, J. L., Leibensperger, E. M., Lu, Z., Meinders, M. B. J., Pye, H. O. T., Quinn, P. K., Sharma, S., Streets, D. G., Donkelaar, A. van, and Yantosca, R. M.: Sources, distribution, and acidity of sulfate–ammonium aerosol in the Arctic in winter–spring, Atmospheric Environment, 45, 7301–7318, https://doi.org/10.1016/j.atmosenv.2011.08.030, 2011.

Giglio, L., Randerson, J. T., and van der Werf, G. R.: Analysis of daily, monthly, and annual burned area using the fourth-generation global fire emissions database (GFED4), Journal of Geophysical Research: Biogeosciences, 118, 317–328, https://doi.org/10.1002/jgrg.20042, 2013.

Giles, D. M., Sinyuk, A., Sorokin, M. G., Schafer, J. S., Smirnov, A., Slutsker, I., Eck, T. F., Holben, B. N., Lewis, J. R., Campbell, J. R., Welton, E. J., Korkin, S. V., and Lyapustin, A. I.: Advancements in the Aerosol Robotic Network (AERONET) Version 3 database – automated near-real-time quality control algorithm with improved cloud screening for Sun photometer aerosol optical depth (AOD) measurements, Atmospheric Measurement Techniques, 12, 169–209, https://doi.org/10.5194/amt-12-169-2019, 2019.

Ginoux, P., Chin, M., Tegen, I., Prospero, J. M., Holben, B., Dubovik, O., and Lin, S.-J.: Sources and distributions of dust aerosols simulated with the GOCART model, Journal of Geophysical Research: Atmospheres, 106, 20255–20273, https://doi.org/10.1029/2000JD000053, 2001.

González-Flórez, C., Klose, M., Alastuey, A., Dupont, S., Escribano, J., Etyemezian, V., Gonzalez-Romero, A., Huang, Y., Kandler, K., Nikolich, G., Panta, A., Querol, X., Reche, C., Yus-Díez, J., and Pérez García-Pando, C.: Insights into the size-resolved dust emission from field measurements in the Moroccan Sahara, Atmospheric Chemistry and Physics, 23, 7177–7212, https://doi.org/10.5194/acp-23-7177-2023, 2023.

Harris, L., Zhou, L., Lin, S.-J., Chen, J.-H., Chen, X., Gao, K., Morin, M., Rees, S., Sun, Y., Tong, M., Xiang, B., Bender, M., Benson, R., Cheng, K.-Y., Clark, S., Elbert, O. D., Hazelton, A., Huff, J. J., Kaltenbaugh, A., Liang, Z., Marchok, T., Shin, H. H., and Stern, W.: GFDL SHiELD: A Unified System for Weather-to-Seasonal Prediction, Journal of Advances in Modeling Earth Systems, 12, e2020MS002223, https://doi.org/10.1029/2020MS002223, 2020.

Hsu, N. C., Lee, J., Sayer, A. M., Kim, W., Bettenhausen, C., and Tsay, S.-C.: VIIRS Deep Blue Aerosol Products Over Land: Extending the EOS Long-Term Aerosol Data Records, Journal of Geophysical Research: Atmospheres, 124, 4026–4053, https://doi.org/10.1029/2018JD029688, 2019.

Hu, L., Keller, C. A., Long, M. S., Sherwen, T., Auer, B., Da Silva, A., Nielsen, J. E., Pawson, S., Thompson, M. A., Trayanov, A. L., Travis, K. R., Grange, S. K., Evans, M. J., and Jacob, D. J.: Global simulation of tropospheric chemistry at 12.5 km resolution: performance and evaluation of the GEOS-Chem chemical module (v10-1) within the NASA GEOS Earth system model (GEOS-5 ESM), Geoscientific Model Development, 11, 4603–4620, https://doi.org/10.5194/gmd-11-4603-2018, 2018.

Huang, Y., Kok, J. F., Kandler, K., Lindqvist, H., Nousiainen, T., Sakai, T., Adebiyi, A., and Jokinen, O.: Climate Models and Remote Sensing Retrievals Neglect Substantial Desert Dust Asphericity, Geophysical Research Letters, 47, e2019GL086592, https://doi.org/10.1029/2019GL086592, 2020.

Huang, Y., Adebiyi, A. A., Formenti, P., and Kok, J. F.: Linking the Different Diameter Types of Aspherical Desert Dust Indicates That Models Underestimate Coarse Dust Emission, Geophysical Research Letters, 48, e2020GL092054, https://doi.org/10.1029/2020GL092054, 2021.

Huneeus, N., Schulz, M., Balkanski, Y., Griesfeller, J., Prospero, J., Kinne, S., Bauer, S., Boucher, O., Chin, M., Dentener, F., Diehl, T., Easter, R., Fillmore, D., Ghan, S., Ginoux, P., Grini, A., Horowitz, L., Koch, D., Krol, M. C., Landing, W., Liu, X., Mahowald, N., Miller, R., Morcrette, J.-J., Myhre, G., Penner, J., Perlwitz, J., Stier, P., Takemura, T., and Zender, C. S.: Global dust model

intercomparison in AeroCom phase I, Atmospheric Chemistry and Physics, 11, 7781–7816, https://doi.org/10.5194/acp-11-7781-2011, 2011.

Iversen, J. D. and White, B. R.: Saltation threshold on Earth, Mars and Venus, Sedimentology, 29, 111–119, https://doi.org/10.1111/j.1365-3091.1982.tb01713.x, 1982.

Jaeglé, L., Quinn, P. K., Bates, T. S., Alexander, B., and Lin, J.-T.: Global distribution of sea salt aerosols: new constraints from in situ and remote sensing observations, Atmospheric Chemistry and Physics, 11, 3137–3157, https://doi.org/10.5194/acp-11-3137-2011, 2011.

Jickells, T. D., An, Z. S., Andersen, K. K., Baker, A. R., Bergametti, G., Brooks, N., Cao, J. J., Boyd, P. W., Duce, R. A., Hunter, K. A., Kawahata, H., Kubilay, N., laRoche, J., Liss, P. S., Mahowald, N., Prospero, J. M., Ridgwell, A. J., Tegen, I., and Torres, R.: Global Iron Connections Between Desert Dust, Ocean Biogeochemistry, and Climate, Science, 308, 67–71, https://doi.org/10.1126/science.1105959, 2005.

Jones, A. C., Hill, A., Hemmings, J., Lemaitre, P., Quérel, A., Ryder, C. L., and Woodward, S.: Below-cloud scavenging of aerosol by rain: a review of numerical modelling approaches and sensitivity simulations with mineral dust in the Met Office's Unified Model, Atmospheric Chemistry and Physics, 22, 11381–11407, https://doi.org/10.5194/acp-22-11381-2022, 2022.

Kenny, L. C., Gussman, R., and Meyer, M.: Development of a Sharp-Cut Cyclone for Ambient Aerosol Monitoring Applications, Aerosol Science and Technology, 32, 338–358, https://doi.org/10.1080/027868200303669, 2000.

Kok, J. F.: A scaling theory for the size distribution of emitted dust aerosols suggests climate models underestimate the size of the global dust cycle, Proceedings of the National Academy of Sciences, 108, 1016–1021, https://doi.org/10.1073/pnas.1014798108, 2011.

Kok, J. F., Mahowald, N. M., Fratini, G., Gillies, J. A., Ishizuka, M., Leys, J. F., Mikami, M., Park, M.-S., Park, S.-U., Van Pelt, R. S., and Zobeck, T. M.: An improved dust emission model – Part 1: Model description and comparison against measurements, Atmospheric Chemistry and Physics, 14, 13023–13041, https://doi.org/10.5194/acp-14-13023-2014, 2014.

Kok, J. F., Ridley, D. A., Zhou, Q., Miller, R. L., Zhao, C., Heald, C. L., Ward, D. S., Albani, S., and Haustein, K.: Smaller desert dust cooling effect estimated from analysis of dust size and abundance, Nature Geoscience, 10, 274–278, https://doi.org/10.1038/ngeo2912, 2017.

Kok, J. F., Adebiyi, A. A., Albani, S., Balkanski, Y., Checa-Garcia, R., Chin, M., Colarco, P. R., Hamilton, D. S., Huang, Y., Ito, A., Klose, M., Li, L., Mahowald, N. M., Miller, R. L., Obiso, V., Pérez García-Pando, C., Rocha-Lima, A., and Wan, J. S.: Contribution of the world's main dust source regions to the global cycle of desert dust, Atmos. Chem. Phys., 21, 8169–8193, https://doi.org/10.5194/acp-21-8169-2021, 2021a.

Kok, J. F., Adebiyi, A. A., Albani, S., Balkanski, Y., Checa-Garcia, R., Chin, M., Colarco, P. R., Hamilton, D. S., Huang, Y., Ito, A., Klose, M., Leung, D. M., Li, L., Mahowald, N. M., Miller, R. L., Obiso, V., Pérez García-Pando, C., Rocha-Lima, A., Wan, J. S., and Whicker, C. A.: Improved representation of the global dust cycle using observational constraints on dust properties and abundance, Atmospheric Chemistry and Physics, 21, 8127–8167, https://doi.org/10.5194/acp-21-8127-2021, 2021b.

Koster, R. D., Reichle, R. H., Mahanama, S. P., Perket, J., Liu, Q., and Partyka, G.: Land-focused changes in the updated GEOS FP system (Version 5.25), 2020.

Latimer, R. N. C. and Martin, R. V.: Interpretation of measured aerosol mass scattering efficiency over North America using a chemical transport model, Atmospheric Chemistry and Physics, 19, 2635–2653, https://doi.org/10.5194/acp-19-2635-2019, 2019.

Leung, D. M., Kok, J. F., Li, L., Okin, G. S., Prigent, C., Klose, M., Pérez García-Pando, C., Menut, L., Mahowald, N. M., Lawrence, D. M., and Chamecki, M.: A new process-based and scale-aware desert dust emission scheme for global climate models – Part I: Description and evaluation against inverse modeling emissions, Atmospheric Chemistry and Physics, 23, 6487–6523, https://doi.org/10.5194/acp-23-6487-2023, 2023.

Leung, D. M., Kok, J. F., Li, L., Mahowald, N. M., Lawrence, D. M., Tilmes, S., Kluzek, E., Klose, M., and Pérez García-Pando, C.: A new process-based and scale-aware desert dust emission scheme for global climate models – Part II: Evaluation in the Community Earth System Model version 2 (CESM2), Atmospheric Chemistry and Physics, 24, 2287–2318, https://doi.org/10.5194/acp-24-2287-2024, 2024.

Li, C., Martin, R. V., van Donkelaar, A., Boys, B. L., Hammer, M. S., Xu, J.-W., Marais, E. A., Reff, A., Strum, M., Ridley, D. A., Crippa, M., Brauer, M., and Zhang, Q.: Trends in Chemical Composition of Global and Regional Population-Weighted Fine Particulate Matter Estimated for 25 Years, Environ. Sci. Technol., 51, 11185–11195, https://doi.org/10.1021/acs.est.7b02530, 2017.

Li, L., Mahowald, N. M., Kok, J. F., Liu, X., Wu, M., Leung, D. M., Hamilton, D. S., Emmons, L. K., Huang, Y., Sexton, N., Meng, J., and Wan, J.: Data and codes for "Importance of different parameterization changes for the updated dust cycle modelling in the Community Atmosphere Model (version 6.1)," https://doi.org/10.5281/zenodo.6989502, 2022a.

Li, L., Mahowald, N. M., Kok, J. F., Liu, X., Wu, M., Leung, D. M., Hamilton, D. S., Emmons, L. K., Huang, Y., Sexton, N., Meng, J., and Wan, J.: Importance of different parameterization changes for the updated dust cycle modeling in the Community Atmosphere Model (version 6.1), Geoscientific Model Development, 15, 8181–8219, https://doi.org/10.5194/gmd-15-8181-2022, 2022b.

Liao, H. and Seinfeld, J. H.: Radiative forcing by mineral dust aerosols: Sensitivity to key variables, Journal of Geophysical Research: Atmospheres, 103, 31637–31645, https://doi.org/10.1029/1998JD200036, 1998.

Lin, H., Jacob, D. J., Lundgren, E. W., Sulprizio, M. P., Keller, C. A., Fritz, T. M., Eastham, S. D., Emmons, L. K., Campbell, P. C., Baker, B., Saylor, R. D., and Montuoro, R.: Harmonized Emissions Component (HEMCO) 3.0 as a versatile emissions component for atmospheric models: application in the GEOS-Chem, NASA GEOS, WRF-GC, CESM2, NOAA GEFS-Aerosol, and NOAA UFS models, Geosci. Model Dev., 14, 5487–5506, https://doi.org/10.5194/gmd-14-5487-2021, 2021.

Liu, H., Jacob, D. J., Bey, I., and Yantosca, R. M.: Constraints from 210Pb and 7Be on wet deposition and transport in a global three-dimensional chemical tracer model driven by assimilated meteorological fields, Journal of Geophysical Research: Atmospheres, 106, 12109–12128, https://doi.org/10.1029/2000JD900839, 2001.

Liu, X., Turner, J. R., Hand, J. L., Schichtel, B. A., and Martin, R. V.: A Global-Scale Mineral Dust Equation, Journal of Geophysical Research: Atmospheres, 127, e2022JD036937, https://doi.org/10.1029/2022JD036937, 2022.

Liu, X., Turner, J. R., Oxford, C. R., McNeill, J., Walsh, B., Le Roy, E., Weagle, C. L., Stone, E., Zhu, H., Liu, W., Wei, Z., Hyslop, N. P., Giacomo, J., Dillner, A. M., Salam, A., Hossen, A., Islam, Z., Abboud, I., Akoshile, C., Amador-Muñoz, O., Anh, N. X., Asfaw, A., Balasubramanian, R., Chang, R. Y.-W., Coburn, C., Dey, S., Diner, D. J., Dong, J., Farrah, T., Gahungu, P., Garland, R. M., Grutter de la Mora, M., Hasheminassab, S., John, J., Kim, J., Kim, J. S., Langerman, K., Lee, P.-C., Lestari, P., Liu, Y., Mamo, T., Martins, M., Mayol-Bracero, O. L., Naidoo, M., Park, S. S., Schechner, Y., Schofield, R., Tripathi, S. N., Windwer, E., Wu, M.-T., Zhang, Q., Brauer, M., Rudich, Y., and Martin,

R. V.: Elemental Characterization of Ambient Particulate Matter for a Globally Distributed Monitoring Network: Methodology and Implications, ACS EST Air, 1, 283–293, https://doi.org/10.1021/acsestair.3c00069, 2024.

Mahowald, N., Kohfeld, K., Hansson, M., Balkanski, Y., Harrison, S. P., Prentice, I. C., Schulz, M., and Rodhe, H.: Dust sources and deposition during the last glacial maximum and current climate: A comparison of model results with paleodata from ice cores and marine sediments, Journal of Geophysical Research: Atmospheres, 104, 15895–15916, https://doi.org/10.1029/1999JD900084, 1999.

Mahowald, N., Albani, S., Kok, J. F., Engelstaeder, S., Scanza, R., Ward, D. S., and Flanner, M. G.: The size distribution of desert dust aerosols and its impact on the Earth system, Aeolian Research, 15, 53–71, https://doi.org/10.1016/j.aeolia.2013.09.002, 2014.

Marticorena, B. and Bergametti, G.: Modeling the atmospheric dust cycle: 1. Design of a soil-derived dust emission scheme, Journal of Geophysical Research: Atmospheres, 100, 16415–16430, https://doi.org/10.1029/95JD00690, 1995.

Martin, R. L. and Kok, J. F.: Distinct Thresholds for the Initiation and Cessation of Aeolian Saltation From Field Measurements, Journal of Geophysical Research: Earth Surface, 123, 1546–1565, https://doi.org/10.1029/2017JF004416, 2018.

Martin, R. V., Eastham, S. D., Bindle, L., Lundgren, E. W., Clune, T. L., Keller, C. A., Downs, W., Zhang, D., Lucchesi, R. A., Sulprizio, M. P., Yantosca, R. M., Li, Y., Estrada, L., Putman, W. M., Auer, B. M., Trayanov, A. L., Pawson, S., and Jacob, D. J.: Improved advection, resolution, performance, and community access in the new generation (version 13) of the high-performance GEOS-Chem global atmospheric chemistry model (GCHP), Geoscientific Model Development, 15, 8731–8748, https://doi.org/10.5194/gmd-15-8731-2022, 2022.

Meng, J., Martin, R. V., Ginoux, P., Hammer, M., Sulprizio, M. P., Ridley, D. A., and van Donkelaar, A.: Grid-independent high-resolution dust emissions (v1.0) for chemical transport models: application to GEOS-Chem (12.5.0), Geoscientific Model Development, 14, 4249–4260, https://doi.org/10.5194/gmd-14-4249-2021, 2021.

Meng, J., Huang, Y., Leung, D. M., Li, L., Adebiyi, A. A., Ryder, C. L., Mahowald, N. M., and Kok, J. F.: Improved Parameterization for the Size Distribution of Emitted Dust Aerosols Reduces Model

Underestimation of Super Coarse Dust, Geophysical Research Letters, 49, e2021GL097287, https://doi.org/10.1029/2021GL097287, 2022.

Miller, S. J., Makar, P. A., and Lee, C. J.: HETerogeneous vectorized or Parallel (HETPv1.0): an updated inorganic heterogeneous chemistry solver for the metastable-state NH_4^+–Na^+–Ca^{2+}–K^+–Mg^{2+}–SO_4^{2-}–NO_3^-–Cl^-–H_2O system based on ISORROPIA II, Geoscientific Model Development, 17, 2197–2219, https://doi.org/10.5194/gmd-17-2197-2024, 2024.

Murray, L. T., Jacob, D. J., Logan, J. A., Hudman, R. C., and Koshak, W. J.: Optimized regional and interannual variability of lightning in a global chemical transport model constrained by LIS/OTD satellite data, Journal of Geophysical Research: Atmospheres, 117, D20307, https://doi.org/10.1029/2012JD017934, 2012.

Mytilinaios, M., Basart, S., Ciamprone, S., Cuesta, J., Dema, C., Di Tomaso, E., Formenti, P., Gkikas, A., Jorba, O., Kahn, R., Pérez García-Pando, C., Trippetta, S., and Mona, L.: Comparison of dust optical depth from multi-sensor products and MONARCH (Multiscale Online Non-hydrostatic AtmospheRe CHemistry) dust reanalysis over North Africa, the Middle East, and Europe, Atmospheric Chemistry and Physics, 23, 5487–5516, https://doi.org/10.5194/acp-23-5487-2023, 2023.

Okin, G. S.: A new model of wind erosion in the presence of vegetation, Journal of Geophysical Research: Earth Surface, 113, https://doi.org/10.1029/2007JF000758, 2008.

Pai, S. J., Heald, C. L., Pierce, J. R., Farina, S. C., Marais, E. A., Jimenez, J. L., Campuzano-Jost, P., Nault, B. A., Middlebrook, A. M., Coe, H., Shilling, J. E., Bahreini, R., Dingle, J. H., and Vu, K.: An evaluation of global organic aerosol schemes using airborne observations, Atmospheric Chemistry and Physics, 20, 2637–2665, https://doi.org/10.5194/acp-20-2637-2020, 2020.

Panofsky, H. A., Tennekes, H., Lenschow, D. H., and Wyngaard, J. C.: The characteristics of turbulent velocity components in the surface layer under convective conditions, Boundary-Layer Meteorology, 11, 355–361, https://doi.org/10.1007/BF02186086, 1977.

Park, R. J., Jacob, D. J., Field, B. D., Yantosca, R. M., and Chin, M.: Natural and transboundary pollution influences on sulfate-nitrate-ammonium aerosols in the United States: Implications for policy, Journal of Geophysical Research: Atmospheres, 109, D15204, https://doi.org/10.1029/2003jd004473, 2004.

Peters, T. M., Kenny, L. C., Gussman, R. A., and Vanderpool, R. W.: Evaluation of PM2.5 Size Selectors Used in Speciation Samplers, Aerosol Science and Technology, 34, 422–429, https://doi.org/10.1080/02786820119266, 2001.

Petroff, A. and Zhang, L.: Development and validation of a size-resolved particle dry deposition scheme for application in aerosol transport models, Geoscientific Model Development, 3, 753–769, https://doi.org/10.5194/gmd-3-753-2010, 2010.

Philip, S., Martin, R. V., Snider, G., Weagle, C. L., Donkelaar, A. van, Brauer, M., Henze, D. K., Klimont, Z., Venkataraman, C., Guttikunda, S. K., and Zhang, Q.: Anthropogenic fugitive, combustion and industrial dust is a significant, underrepresented fine particulate matter source in global atmospheric models, Environmental Research Letters, 12, 044018, https://doi.org/10.1088/1748-9326/aa65a4, 2017.

Pierre, C., Bergametti, G., Marticorena, B., Kergoat, L., Mougin, E., and Hiernaux, P.: Comparing drag partition schemes over a herbaceous Sahelian rangeland, Journal of Geophysical Research: Earth Surface, 119, 2291–2313, https://doi.org/10.1002/2014JF003177, 2014a.

Pierre, C., Bergametti, G., Marticorena, B., AbdourhamaneTouré, A., Rajot, J.-L., and Kergoat, L.: Modeling wind erosion flux and its seasonality from a cultivated sahelian surface: A case study in Niger, CATENA, 122, 61–71, https://doi.org/10.1016/j.catena.2014.06.006, 2014b.

Poggio, L., de Sousa, L. M., Batjes, N. H., Heuvelink, G. B. M., Kempen, B., Ribeiro, E., and Rossiter, D.: SoilGrids 2.0: producing soil information for the globe with quantified spatial uncertainty, SOIL, 7, 217–240, https://doi.org/10.5194/soil-7-217-2021, 2021.

Prigent, C., Tegen, I., Aires, F., Marticorena, B., and Zribi, M.: Estimation of the aerodynamic roughness length in arid and semi-arid regions over the globe with the ERS scatterometer, Journal of Geophysical Research: Atmospheres, 110, https://doi.org/10.1029/2004JD005370, 2005.

Prospero, J. M.: Long-range transport of mineral dust in the global atmosphere: Impact of African dust on the environment of the southeastern United States, Proceedings of the National Academy of Sciences, 96, 3396–3403, https://doi.org/10.1073/pnas.96.7.3396, 1999.

Reid, J. S., Jonsson, H. H., Maring, H. B., Smirnov, A., Savoie, D. L., Cliff, S. S., Reid, E. A., Livingston, J. M., Meier, M. M., Dubovik, O., and Tsay, S.-C.: Comparison of size and morphological measurements of coarse mode dust particles from Africa, Journal of Geophysical Research:

Atmospheres, 108, https://doi.org/10.1029/2002JD002485, 2003.

Ridley, D. A., Heald, C. L., and Ford, B.: North African dust export and deposition: A satellite and model perspective, Journal of Geophysical Research: Atmospheres, 117, D02202, https://doi.org/10.1029/2011JD016794, 2012.

Ridley, D. A., Heald, C. L., Kok, J. F., and Zhao, C.: An observationally constrained estimate of global dust aerosol optical depth, Atmospheric Chemistry and Physics, 16, 15097–15117, https://doi.org/10.5194/acp-16-15097-2016, 2016.

Ryder, C. L., Highwood, E. J., Rosenberg, P. D., Trembath, J., Brooke, J. K., Bart, M., Dean, A., Crosier, J., Dorsey, J., Brindley, H., Banks, J., Marsham, J. H., McQuaid, J. B., Sodemann, H., and Washington, R.: Optical properties of Saharan dust aerosol and contribution from the coarse mode as measured during the Fennec 2011 aircraft campaign, Atmospheric Chemistry and Physics, 13, 303–325, https://doi.org/10.5194/acp-13-303-2013, 2013.

Ryu, Y.-H. and Min, S.-K.: Improving Wet and Dry Deposition of Aerosols in WRF-Chem: Updates to Below-Cloud Scavenging and Coarse-Particle Dry Deposition, Journal of Advances in Modeling Earth Systems, 14, e2021MS002792, https://doi.org/10.1029/2021MS002792, 2022.

Shangguan, W., Dai, Y., Duan, Q., Liu, B., and Yuan, H.: A global soil data set for earth system modeling, Journal of Advances in Modeling Earth Systems, 6, 249–263, https://doi.org/10.1002/2013MS000293, 2014.

Shao, Y. and Lu, H.: A simple expression for wind erosion threshold friction velocity, Journal of Geophysical Research: Atmospheres, 105, 22437–22443, https://doi.org/10.1029/2000JD900304, 2000.

Singh, I., Martin, R. V., Bindle, L., Chatterjee, D., Li, C., Oxford, C., Xu, X., and Wang, J.: Effect of Dust Morphology on Aerosol Optics in the GEOS-Chem Chemical Transport Model, on UV-Vis Trace Gas Retrievals, and on Surface Area Available for Reactive Uptake, Journal of Advances in Modeling Earth Systems, 16, e2023MS003746, https://doi.org/10.1029/2023MS003746, 2024.

Sinyuk, A., Torres, O., and Dubovik, O.: Combined use of satellite and surface observations to infer the imaginary part of refractive index of Saharan dust, Geophysical Research Letters, 30, https://doi.org/10.1029/2002GL016189, 2003.

Smith, R. J.: Use and misuse of the reduced major axis for line-fitting, American Journal of Physical Anthropology, 140, 476–486, https://doi.org/10.1002/ajpa.21090, 2009.

Snider, G., Weagle, C. L., Martin, R. V., van Donkelaar, A., Conrad, K., Cunningham, D., Gordon, C., Zwicker, M., Akoshile, C., Artaxo, P., Anh, N. X., Brook, J., Dong, J., Garland, R. M., Greenwald, R., Griffith, D., He, K., Holben, B. N., Kahn, R., Koren, I., Lagrosas, N., Lestari, P., Ma, Z., Vanderlei Martins, J., Quel, E. J., Rudich, Y., Salam, A., Tripathi, S. N., Yu, C., Zhang, Q., Zhang, Y., Brauer, M., Cohen, A., Gibson, M. D., and Liu, Y.: SPARTAN: a global network to evaluate and enhance satellite-based estimates of ground-level particulate matter for global health applications, Atmospheric Measurement Techniques, 8, 505–521, https://doi.org/10.5194/amt-8-505-2015, 2015.

Song, Q., Zhang, Z., Yu, H., Ginoux, P., and Shen, J.: Global dust optical depth climatology derived from CALIOP and MODIS aerosol retrievals on decadal timescales: regional and interannual variability, Atmospheric Chemistry and Physics, 21, 13369–13395, https://doi.org/10.5194/acp-21-13369-2021, 2021.

Swap, R., Garstang, M., Greco, S., Talbot, R., and Kallberg, P.: Saharan dust in the Amazon Basin, Tellus B, 44, 133–149, https://doi.org/10.1034/j.1600-0889.1992.t01-1-00005.x, 1992.

Swenson, S. C. and Lawrence, D. M.: Assessing a dry surface layer-based soil resistance parameterization for the Community Land Model using GRACE and FLUXNET-MTE data, Journal of Geophysical Research: Atmospheres, 119, 10,299-10,312, https://doi.org/10.1002/2014JD022314, 2014.

The International GEOS-Chem User Community: geoschem/GCHP: GCHP 14.4.1, , https://doi.org/10.5281/zenodo.12584305, 2024.

Tian, R., Ma, X., and Zhao, J.: A revised mineral dust emission scheme in GEOS-Chem: improvements in dust simulations over China, Atmospheric Chemistry and Physics, 21, 4319–4337, https://doi.org/10.5194/acp-21-4319-2021, 2021.

Tindan, J. Z., Jin, Q., and Pu, B.: Understanding day–night differences in dust aerosols over the dust belt of North Africa, the Middle East, and Asia, Atmos. Chem. Phys., 23, 5435–5466, https://doi.org/10.5194/acp-23-5435-2023, 2023.

Uno, I., Wang, Z., Chiba, M., Chun, Y. S., Gong, S. L., Hara, Y., Jung, E., Lee, S.-S., Liu, M., Mikami, M., Music, S., Nickovic, S., Satake, S., Shao, Y., Song, Z., Sugimoto, N., Tanaka, T., and Westphal,

D. L.: Dust model intercomparison (DMIP) study over Asia: Overview, Journal of Geophysical Research: Atmospheres, 111, https://doi.org/10.1029/2005JD006575, 2006.

Wang, Q., Jacob, D. J., Fisher, J. A., Mao, J., Leibensperger, E. M., Carouge, C. C., Le Sager, P., Kondo, Y., Jimenez, J. L., Cubison, M. J., and Doherty, S. J.: Sources of carbonaceous aerosols and deposited black carbon in the Arctic in winter-spring: implications for radiative forcing, Atmospheric Chemistry and Physics, 11, 12453–12473, https://doi.org/10.5194/acp-11-12453-2011, 2011.

Wang, Q., Jacob, D. J., Spackman, J. R., Perring, A. E., Schwarz, J. P., Moteki, N., Marais, E. A., Ge, C., Wang, J., and Barrett, S. R. H.: Global budget and radiative forcing of black carbon aerosol: Constraints from pole-to-pole (HIPPO) observations across the Pacific, Journal of Geophysical Research: Atmospheres, 119, 195–206, https://doi.org/10.1002/2013jd020824, 2014a.

Wang, X., Zhang, L., and Moran, M. D.: Development of a new semi-empirical parameterization for below-cloud scavenging of size-resolved aerosol particles by both rain and snow, Geoscientific Model Development, 7, 799–819, https://doi.org/10.5194/gmd-7-799-2014, 2014b.

Wang, X., Jacob, D. J., Downs, W., Zhai, S., Zhu, L., Shah, V., Holmes, C. D., Sherwen, T., Alexander, B., Evans, M. J., Eastham, S. D., Neuman, J. A., Veres, P. R., Koenig, T. K., Volkamer, R., Huey, L. G., Bannan, T. J., Percival, C. J., Lee, B. H., and Thornton, J. A.: Global tropospheric halogen (Cl, Br, I) chemistry and its impact on oxidants, Atmospheric Chemistry and Physics, 21, 13973–13996, https://doi.org/10.5194/acp-21-13973-2021, 2021.

Webb, N. P., Chappell, A., LeGrand, S. L., Ziegler, N. P., and Edwards, B. L.: A note on the use of drag partition in aeolian transport models, Aeolian Research, 42, 100560, https://doi.org/10.1016/j.aeolia.2019.100560, 2020.

Weng, H., Lin, J., Martin, R. V., Millet, D. B., Jaeglé, L., Ridley, D., Keller, C., Li, C., Du, M., and Meng, J.: Global high-resolution emissions of soil NO_x, sea salt aerosols, and biogenic volatile organic compounds, Scientific Data, 7, 148, https://doi.org/10.1038/s41597-020-0488-5, 2020.

Wu, C., Lin, Z., and Liu, X.: The global dust cycle and uncertainty in CMIP5 (Coupled Model Intercomparison Project phase 5) models, Atmospheric Chemistry and Physics, 20, 10401–10425, https://doi.org/10.5194/acp-20-10401-2020, 2020.

Wu, C., Lin, Z., Shao, Y., Liu, X., and Li, Y.: Drivers of recent decline in dust activity over East Asia,

Nature Communications, 13, 7105, https://doi.org/10.1038/s41467-022-34823-3, 2022.

Young, S. A., Vaughan, M. A., Garnier, A., Tackett, J. L., Lambeth, J. D., and Powell, K. A.: Extinction and optical depth retrievals for CALIPSO's Version 4 data release, Atmospheric Measurement Techniques, 11, 5701–5727, https://doi.org/10.5194/amt-11-5701-2018, 2018.

Yu, Y., Kalashnikova, O. V., Garay, M. J., Lee, H., Choi, M., Okin, G. S., Yorks, J. E., Campbell, J. R., and Marquis, J.: A global analysis of diurnal variability in dust and dust mixture using CATS observations, Atmos. Chem. Phys., 21, 1427–1447, https://doi.org/10.5194/acp-21-1427-2021, 2021.

Yuan, H., Dai, Y., Xiao, Z., Ji, D., and Shangguan, W.: Reprocessing the MODIS Leaf Area Index products for land surface and climate modelling, Remote Sensing of Environment, 115, 1171–1187, https://doi.org/10.1016/j.rse.2011.01.001, 2011.

Zender, C. S., Bian, H., and Newman, D.: Mineral Dust Entrainment and Deposition (DEAD) model: Description and 1990s dust climatology, Journal of Geophysical Research: Atmospheres, 108, https://doi.org/10.1029/2002JD002775, 2003.

Zhang, D.: Improving Fine Mineral Dust Representation from the Surface to the Column in GEOS-Chem version 14.4.1, https://doi.org/10.5281/zenodo.14510793, 2024.

Zhang, J. and Shao, Y.: A new parameterization of particle dry deposition over rough surfaces, Atmospheric Chemistry and Physics, 14, 12429–12440, https://doi.org/10.5194/acp-14-12429-2014, 2014.

Zhang, L., Gong, S., Padro, J., and Barrie, L.: A size-segregated particle dry deposition scheme for an atmospheric aerosol module, Atmospheric Environment, 35, 549–560, https://doi.org/10.1016/S1352-2310(00)00326-5, 2001.

Zhang, L., Kok, J. F., Henze, D. K., Li, Q., and Zhao, C.: Improving simulations of fine dust surface concentrations over the western United States by optimizing the particle size distribution, Geophysical Research Letters, 40, 3270–3275, https://doi.org/10.1002/grl.50591, 2013.

Zhao, A., Ryder, C. L., and Wilcox, L. J.: How well do the CMIP6 models simulate dust aerosols?, Atmos. Chem. Phys., 22, 2095–2119, https://doi.org/10.5194/acp-22-2095-2022, 2022.

Zhu, H., Martin, R. V., Croft, B., Zhai, S., Li, C., Bindle, L., Pierce, J. R., Chang, R. Y.-W., Anderson, B.

E., Ziemba, L. D., Hair, J. W., Ferrare, R. A., Hostetler, C. A., Singh, I., Chatterjee, D., Jimenez, J. L., Campuzano-Jost, P., Nault, B. A., Dibb, J. E., Schwarz, J. S., and Weinheimer, A.: Parameterization of size of organic and secondary inorganic aerosol for efficient representation of global aerosol optical properties, Atmospheric Chemistry and Physics, 23, 5023–5042, https://doi.org/10.5194/acp-23-5023-2023, 2023.